# Transition scenario to turbulence in thin vibrating plates

Cyril Touzé, Stefan Bilbao, Olivier Cadot

# Transition scenario to turbulence in thin vibrating plates

C. Touzé[a,*], S. Bilbao[b], O. Cadot[a]

[a] *Unité de Mécanique (UME), ENSTA-ParisTech, Chemin de la Hunière, 91761 Palaiseau Cedex, France*
[b] *Acoustics and Fluid Dynamics Group/Music, University of Edinburgh, James Clerk Maxwell Building, Edinburgh, United Kingdom*

**Abstract**

A thin plate, excited by a harmonic external forcing of increasing amplitude, shows transitions from a periodic response to a chaotic state of wave turbulence. By analogy with the transition to turbulence observed in fluid mechanics as the Reynolds number is increased, a generic transition scenario for thin vibrating plates, first experimentally observed, is here numerically studied. The von Kármán equations for thin plates, which include geometric non-linear effects, are used to model large amplitude vibrations, and an energy-conserving finite difference scheme is employed for discretization. The transition scenario involves two bifurcations separating three distinct regimes. The first regime is the periodic, weakly non-linear response. The second is a quasiperiodic state where energy is exchanged between internally resonant modes. It is observed only when specific internal resonance relationships are fulfilled between the eigenfrequencies of the structure and the forcing frequency; otherwise a direct transition to the last turbulent state is observed. This third, or turbulent, regime is characterized by a broadband Fourier spectrum and a cascade of energy from large to small wavelengths. For perfect plates including cubic non-linearity, only third-order internal resonances are likely to exist. For imperfect plates displaying quadratic nonlinearity, the energy exchanges and the quasiperiodic states are favored and thus are more easily obtained. Finally, the turbulent regime is characterized in the light of available theoretical results from wave turbulence theory.

*Keywords:* transition scenario, thin plate, wave turbulence, bifurcation

## 1. Introduction

*Turbulence and wave turbulence.* Turbulence has always been a key research area in fluid mechanics and is still considered as a partly unsolved (and perhaps unsolvable) problem due to fundamental limitations of analytical tools in the case of an infinite hierarchy of cumulant equations [1, 2]. Zacharov [3], however, introduced a so-called wave (or weak) turbulence (WT) theory which may be arrived at by relaxing some of the assumptions that are particularly relevant to fully developed hydrodynamics turbulence (in particular the presence of intermittency), but by retaining the main assumption of an energy flux through lengthscales allowing for the appearance of the Kolmogorov turbulence spectrum. The main assumptions of WT are that the nonlinearity is weak, and that waves persist in the dynamical behaviour of the system [4]. With this in mind, closed equations, the so-called kinetic equations, are analytically accessible,

*Corresponding author
*Email addresses:* cyril.touze@ensta-paristech.fr (C. Touzé), Stefan.Bilbao@ed.ac.uk (S. Bilbao), olivier.cadot@ensta-paristech.fr (O. Cadot)

and hence allow for quantitative predictions. Because of these tractable simplifications, the WT theory has been applied successfully to numerous physical systems including capillarity and gravity waves on the surface of liquids [5, 6, 7, 8], plasmas [9], optics [10] and magnetohydrodynamics [11].

*Turbulence in a solid.* Wave turbulence theory can be applied to vibrating structures that can display, when subjected to large-amplitude motions under a geometric non-linearity, a broadband Fourier component in the power spectrum of the displacement, revealing turbulent behaviour. In the musical context, the perceptual importance of this feature has been long since recognized in instrument design; for example, the broadband Fourier component has been exploited for a long time in theaters to simulate the sound of thunder by shaking vigorously large metallic plates. It is also the means of explaining the bright shimmering sound of gongs and cymbals [12, 13, 14, 15, 16]. From the physical point of view, this vibration state was first studied in the framework of chaotic behaviour for dynamical systems [17, 14, 18, 19]. However, convergence of traditional indicators of chaotic dynamics resulting from low-dimensional dynamical systems (*e.g.* correlation dimension and Lyapunov exponents) has been found from experiments only recently in a series of papers by Nagai *et al.* [20, 21, 22] where a shell of small dimensions was excited at moderate amplitudes, so that turbulent behaviour is not excited. Other experimental studies [23, 24, 13], as well as numerical results [25] reported difficulties in obtaining converged values for the correlation dimension and/or the Lyapunov exponents. Recently, wave turbulence theory has been applied to vibrating plates described by the von Kármán kinematical assumptions, hence allowing for a quantitative prediction of the energy repartition through lengthscales [26], and two different experimental set-ups with very thin plates of large dimensions precisely accounted for turbulent behaviour [27, 28, 29]. More specifically, no intermittent behaviour was reported [27] and the persistence of waves has been clearly highlighted [29, 30], so that the main assumptions of WT are clearly verified experimentally.

*Goal.* The aim of this paper is to present numerical results allowing the study of the turbulent behaviour of plates, with or without imperfection, and this first part is more directly concerned with the transition to turbulence. First, experimental results indicate the generic transition scenario observed in thin structures like plates and shells, when they are excited pointwise with a harmonic forcing of increasing amplitude. This scenario has already been reported elsewhere for gongs and cymbals [12, 13, 14, 24, 31, 25]; here experimental results on a rectangular plate are presented, showing once again the generality of these observations. Next, a numerical model is presented, allowing for a precise reproduction of the experimental set-up. The model is based on a finite difference scheme that, in the lossless case, conserves energy to machine accuracy [32], and allows modelling of pointwise harmonic forcing. Preliminary numerical results have already been presented for a plate with free edges in [33]; here the case of simply-supported edges is considered. The transition scenario is then numerically assessed, for the case of perfect and imperfect plates. Finally, the turbulent state is briefly addressed by comparing the power spectrum of the numerically obtained velocity to that predicted in [26].

*Summary of experimental results.* The case of a thin structure (such as a plate, shell, gong or cymbal) excited pointwise with a harmonic forcing of a given frequency $f^{exc}$ and linearly increasing amplitude, is considered. Numerous observations have already been reported on various kinds of gongs, cymbals and circular spherical-cap shells in [12, 13, 14, 34, 24, 31, 25], where the pointwise forcing is realized either with a mechanical shaker or with an electromagnetic device consisting of a magnet glued to the structure surrounded by a coil with controlled current, as described in [35, 36, 28]. The observed scenario for the transition to turbulence in

vibrating structures implies two bifurcations, separating three distinct regimes.

The case is here illustrated in Fig. 1, showing measurements drawn from a thin rectangular plate of lateral dimensions 38cm×29cm and thickness $h$=1 mm. The plate is excited at its centre by a shaker and has free edges. The vibration velocity is measured by a laser vibrometer, 2 centimeters from the center (to avoid laser saturation if measuring near the edges, as can occur in the turbulent regime where the vibration amplitude can be of the order of one centimeter). Fig. 1 shows two typical measurements obtained for excitation frequencies $f^{exc}$=151 Hz and 290 Hz respectively. The excitation amplitude is increased linearly during the experiment, then maintained at a constant value once the turbulent regime is attained. Spectrograms of the measured velocity are shown, with time indicated on the abscissa.

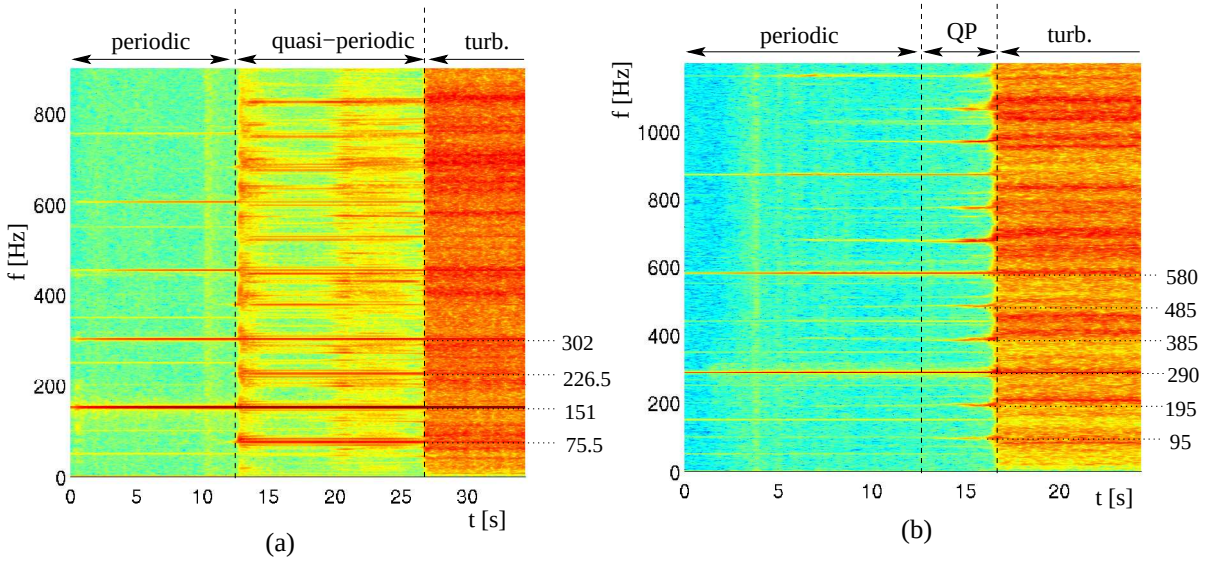


Figure 1: Experimental spectrograms of the vibration velocity for a rectangular plate excited with a harmonic force of increasing amplitude and frequency 151 Hz (a), and 290 Hz (b). In each case the three different vibration regimes are clearly identified.

For small excitation amplitude, the regime is moderately nonlinear. In order to optimize the injection of energy, $f^{exc}$ is generally chosen in the vicinity of one of the structure's linear eigenfrequencies. Hence the first regime is essentially a nonlinear unimodal regime, where the directly excited mode vibrates in the nonlinear regime, characterized by the appearance of harmonics of the forcing in the response. In the two cases, harmonics of order 2 to 4 are clearly visible; as imperfections are unavoidable in real plates [37], quadratic nonlinearity is present, and these even harmonics are observed in the response. Note the presence of harmonics of 50 Hz in the response, at small and constant levels. They are related to the current delivered and are unavoidable in measurements. They are easily recognizable and must not be interpreted as physical.

For a given excitation amplitude level, a bifurcation is observed. In Fig. 1(a), a 1:2 internal resonance is excited, and energy is transferred from the directly excited mode to that with eigenfrequency near $f^{exc}/2$. Modal analysis reveals the existence of an eigenmode at frequency 72 Hz, which is here slightly shifted by the nonlinearity and lock-in phenomena to perfectly fulfill the 1:2 resonance relationship and receive energy from the directly excited mode. The bifurcation is clearly delimited, as is usual in 1:2 internal resonance where a subcritical bifurcation is at hand [38, 39, 40]. Consequently the jump to the coupled branch excites higher

frequencies resulting in a short transient. Then the coupled 1:2 regime sets in clearly, and finally appears to be disturbed in the vicinity of the second bifurcation. For $f^{exc}$= 290 Hz, Fig 1(b), the first regime becomes unstable in favour of a coupled regime involving two eigenmodes, whose eigenfrequencies $f_1$ =95 Hz and $f_2$ =195 Hz are such that $f_1 + f_2 = f^{exc}$, resulting in a 1+1:2 internal resonance relationship. Once again, linear analysis reveals the presence of two eigenmodes at 90 and 190 Hz respectively, again with frequencies slightly shifted to fulfill the resonance condition. From these two examples and those already presented in [13, 14, 25], the generic scenario experimentally observed involves thus a first bifurcation where all the modes sharing internal resonance relationships of the form :

$$f_i + f_j = f^{exc} \tag{1}$$

are excited through energy exchange, leading to a so-called quasiperiodic state. The simple case of 1:2 internal resonance is a particular case of (1) where $f_i = f_j$ leading to a quasiperiodic state degenerated in a periodic regime. The frequency peaks appearing in the quasiperiodic regime can also not be directly related to the excitation frequency. The energy can first be spread through modes sharing internal resonance with the directly excited modes like (1), then, once this new subset of frequencies is excited, new modes sharing a resonance relationship of the form $f_n \pm f_p = f_k$ with at least one of $f_n$, $f_p$ or $f_k$ belonging to the first subset of excited modes, can appear in the vibration. In all the experiments realized, order-two internal resonance relationships have always been observed, which simply reflect the fact that for real plates with imperfections, quadratic nonlinearities dominate those of cubic type, so that order-three internal resonance relationships are completely hidden by those of second order. Fig. 1 shows two excitation frequencies for which the quasiperiodic regime appears, but it may not be present if no evident internal resonance relationships exist. This has been observed preferentially for low-frequency excitations, as the coupling appears to be with modes with frequency smaller than that of the excitation.

Finally, the second bifurcation occurs and the turbulent regime sets in. It is characterized by a broadband Fourier spectrum with energy up to 8000 Hz for the two cases shown in Fig 1, indicating a flux of energy from the injection scale to the dissipative scale.

The aim of this paper is to develop an efficient numerical method in order to study the transition to turbulence through simulations, allowing validation of the scenario inferred from experimental measurements, as well as to give more insight to turbulent behaviour.

## 2. Numerical model

### *2.1. The von Kármán equations for perfect and imperfect plates*

The model chosen here relies on the von Kármán kinematical assumptions for describing the geometric (large-amplitude) non-linear behaviour of thin plates. A rectangular plate of dimensions $L_x \times L_y$ and thickness $h$ is considered, and is of elastic material of density $\rho$, Young's modulus $E$ and Poisson's ratio $\nu$. The equations of motion are given for an imperfect plate without residual stresses, and comprise a set of two equations for the two unknowns, namely the transverse displacement $\bar{w}(x, y, t)$ and the Airy (or stress) function $\bar{F}(x, y, t)$ [41, 42, 43, 37]:

$$\rho h\ddot{\bar{w}} + D\Delta\Delta\bar{w} + \bar{\sigma_0}\dot{\bar{w}} = L(\bar{w}, \bar{F}) + L(\bar{w}_0, \bar{F}) + \bar{p}, \tag{2a}$$

$$\Delta\Delta\bar{F} = -\frac{Eh}{2}[L(\bar{w}, \bar{w}) + 2L(\bar{w}, \bar{w}_0)], \tag{2b}$$

where $D = Eh^3/12(1-\nu^2)$ is the flexural rigidity, $\bar{\sigma_0}$ is an ad hoc viscous damping coefficient, and $\bar{p}$ represents the external forcing applied to the plate. The geometric imperfection is represented by the displacement $\bar{w_0}(x, y, t)$ of the middle surface. In setting $\bar{w_0} = 0$, the von Kármán equations for perfect plates are recovered. The bilinear operator $L$ is defined, in Cartesian coordinates, as:

$$L(F, w) = F_{,xx}w_{,yy} + F_{,yy}w_{,xx} - 2F_{,xy}w_{,xy} \tag{3}$$

The equations (2) are scaled by using the following transformations:

$$x = \frac{\bar{x}}{\sqrt{L_x L_y}}, \qquad y = \frac{\bar{y}}{\sqrt{L_x L_y}}, \qquad w = \frac{\sqrt{6(1-\nu^2)}}{h}\bar{w} \tag{4a}$$

$$F = \frac{\bar{F}}{D}, \qquad \sigma_0 = \frac{\bar{\sigma_0}}{\rho h}, \qquad p = \frac{\sqrt{6(1-\nu^2)}}{\rho h^2}\bar{p} \tag{4b}$$

After substitution, we obtain:

$$\ddot{w} + \kappa^2 \Delta\Delta w + \sigma_0 \dot{w} = \kappa^2 L(w + w_0, F) + p, \tag{5a}$$

$$\Delta\Delta F = -L(w, w + 2w_0), \tag{5b}$$

where $\kappa^2 = \frac{D}{\rho h L_x^2 L_y^2}$. The equations of motion (5) will be used in the remainder of the article. It is worth noting that they are not non-dimensional equations: time has not been scaled, so that the factor $\kappa$ has the dimension of a frequency. This choice has been retained for computational reasons.

In the remainder of the paper, simply supported boundary conditions are chosen. For the scaled transverse displacement $w$, simplified boundary conditions are used [44, 45, 16]:

$$w = 0, \quad \frac{\partial^2 w}{\partial x^2} = 0; \qquad \text{for } x = 0,\ \sqrt{\frac{L_x}{L_y}};\ \forall y \tag{6a}$$

$$w = 0, \quad \frac{\partial^2 w}{\partial y^2} = 0; \qquad \text{for } y = 0,\ \sqrt{\frac{L_y}{L_x}};\ \forall x. \tag{6b}$$

For the scaled Airy stress function $F$ the following boundary conditions have been chosen [45]:

$$F = 0, \quad \frac{\partial F}{\partial x} = 0; \qquad \text{for } x = 0,\ \sqrt{\frac{L_x}{L_y}}; \forall y \tag{7a}$$

$$F = 0, \quad \frac{\partial F}{\partial y} = 0; \qquad \text{for } y = 0,\ \sqrt{\frac{L_x}{L_y}}; \forall x \tag{7b}$$

### *2.2. Finite difference scheme*

In this section a finite difference scheme is introduced to solve the equations of motion (5) together with boundary conditions (6)-(7). The scheme is a perfectly energy-conserving scheme (under lossless conditions), to machine accuracy, and has been introduced in [32]. It is here adapted to the case of forced and damped equations.

*2.2.1. Grid functions and operators*

The main steps for deriving the energy-conserving scheme are here briefly recalled, following the notations and the definitions given in [16, 32]. For more thorough details on the discrete operators, the reader is referred to [16], and to [32] for the proof that the scheme is energy-conserving for undamped and unforced equations.

The continuous unknown functions $w(x, y, t)$ and $F(x, y, t)$ are replaced by their values on a discrete domain: $w^n_{l,m}$ and $F^n_{l,m}$, for integer $l$, $m$ and $n$. The time index is $n$ where continuous time $t$ has been replaced by its discrete counterpart $t_n = nh_t$ with $h_t$ the time step. In the same manner, the spatial domain is discretized so that the indices $l, m$ are defined through: $(l, m) \in [0, N_x] \times [0, N_y]$. The size of the domain is $(N_x + 1)(N_y + 1)$, and the space steps are denoted respectively by $h_x$ and $h_y$. In practice, the grid spacings $h_x$ and $h_y$ are fixed by the stability condition of the scheme (see below), and the number of grid points is deduced from $N_x = E(\frac{1}{h_x}\sqrt{\frac{L_x}{L_y}})$ and $N_y = E(\frac{1}{h_y}\sqrt{\frac{L_y}{L_x}})$, where $E(\tau)$ stands for the integer part of $\tau$. For minimal numerical dispersion effects, it is best to choose the grid spacings as close to these bounds as possible, for a given time step.

The following discrete notations are now introduced. The unit forward and backward time shift operator are defined through their action on a grid function, say $w^n_{l,m}$, as:

$$e_{t^+} w^n_{l,m} = w^{n+1}_{l,m}, \quad e_{t^-} w^n_{l,m} = w^{n-1}_{l,m}. \tag{8}$$

Classical approximations of the first (centered, forward and backward) and second derivatives in time read as:

$$\delta_{t\cdot} = \frac{1}{2h_t}(e_{t^+} - e_{t^-}), \quad \delta_{t^+} = \frac{1}{h_t}(e_{t^+} - 1), \quad \delta_{t^-} = \frac{1}{h_t}(1 - e_{t^-}), \quad \delta_{tt} = \delta_{t^+}\delta_{t^-}, \tag{9}$$

where "1" stands for the identity operator.

Temporal averaging operator are defined as:

$$\mu_{t^+} = \frac{1}{2}(e_{t^+} + 1), \quad \mu_{t^-} = \frac{1}{2}(1 + e_{t^-}), \quad \mu_{t\cdot} = \frac{1}{2}(e_{t^+} + e_{t^-}), \quad \mu_{tt} = \mu_{t^+}\mu_{t^-}, \tag{10}$$

The same definitions clearly follow for the spatial discrete variables, where we will also need a discrete bi-Laplacian (or biharmonic) operator $\delta_{\Delta\Delta}$ defined from:

$$\delta_\Delta = \delta_{xx} + \delta_{yy} \tag{11}$$

$$\delta_{\Delta\Delta} = \delta_\Delta \delta_\Delta \tag{12}$$

*2.2.2. Conservative scheme*

The two-parameter family of energy-conserving schemes (or monotonically dissipative in the lossy case) introduced in [32] is here adapted to the case of the damped and forced problem defined by (5). For the sake of simplicity, the discrete variables $w^n_{l,m}$ and $F^n_{l,m}$ are simply denoted by $w$ and $F$. The family of schemes depends on two parameters named $\beta$ and $\gamma$, as:

$$\delta_{tt} w = -\kappa^2 \delta_{\Delta\Delta} w - \sigma_0 \delta_{t\cdot} w + \kappa^2 l(\tilde{w} + \tilde{w}_0, \tilde{F}) + p^n_{l,m}, \tag{13a}$$

$$\mu_{t^-}\delta_{\Delta\Delta} F = -\gamma l(w, e_{t^-}(w + 2w_0)) - (1 - \gamma)\mu_{t^-} l(w, w + 2w_0). \tag{13b}$$

where the following terms, directly depending on the two parameters $\beta$ and $\gamma$, have been introduced:

$$\tilde{w} = \gamma w + (1 - \gamma)\mu_{t\cdot} w, \tag{14a}$$

$$\tilde{w}_0 = \gamma w_0 + (1 - \gamma)\mu_{t\cdot} w_0, \tag{14b}$$

$$\tilde{F} = \beta F + (1 - \beta)\mu_{t\cdot} F. \tag{14c}$$

The bilinear operator $L$ has been discretized as $l(w, F)$ and reads:

$$l(w, F) = \delta_{xx} w \, \delta_{yy} F + \delta_{yy} w \, \delta_{xx} F - 2\mu_{x^-}\mu_{y^-}(\delta_{x^+y^+} w \, \delta_{x^+y^+} F). \tag{15}$$

The external forcing is introduced so as to mimic the experimental results described in the introduction. Consequently, the dimensioned forcing has been chosen as

$$\bar{p}(\bar{x}, \bar{y}, t) = \delta(\bar{x} - \bar{x}_0)\delta(\bar{y} - \bar{y}_0)\, \bar{A} \sin(\Omega t), \tag{16}$$

where $\bar{A}$ is the amplitude of the forcing (in N), and $\Omega$ the excitation frequency. The non-dimensional forcing simply reads:

$$p(x, y, t) = \delta(x - x_0)\delta(y - y_0)\, A \sin(\Omega t), \quad \text{with } A = \frac{\sqrt{6(1-\nu^2)}}{\rho h^2 L_x L_y} \bar{A} \tag{17}$$

The forcing is pointwise, so that the discretized forcing term $p^n_{l,m}$ appearing in Eq. (13a) is bilinearly spread to the four nearest neighbours of the chosen excitation point $(x_0, y_0)$.

The stability condition, which may be derived through energy analysis, is:

$$\beta \leq 1/2 \tag{18a}$$

$$h_t \leq \frac{h_x^2 h_y^2}{2(h_x^2 + h_y^2)} \sqrt{\frac{\rho h}{D}} \tag{18b}$$

under the choice of $\gamma = 1$ and $\beta = 0$. It is worth emphasizing that this condition, identical to that which holds in the linear case, is here necessary and sufficient for stability in the fully nonlinear case as well.

In practice, the sampling rate $f_S$ is chosen a priori, and the number of grid points for the simulation is chosen so as to satisfy the above condition as closely as possible, thus minimizing numerical dispersion effects.

## 3. Simulation results for the perfect plate

### *3.1. Linear convergence*

For the simulations, a plate has been chosen with dimensions $L_x = 0.4\text{m} \times L_y = 0.6\text{m}$, and thickness $h$=1 mm. Material parameters have been set so as to model a steel plate, with $E$= 200 GPa, $\nu$=0.3 and $\rho$=7860 kg.m$^{-3}$.

For a simply-supported plate, the radian frequencies are known analytically [44]:

$$\omega^a_{pq} = \pi^2 \sqrt{\frac{D}{\rho h}} \left[ \frac{p^2}{L_x^2} + \frac{q^2}{L_y^2} \right], \tag{19}$$

where $p$ and $q$ are two integers indicating the number of half-waves in the $x$ and $y$ directions respectively. Table 1 shows the first 27 exact eigenfrequencies of the chosen plate, ranging from 21.65 Hz (fundamental mode) to 406.29 Hz.

The linear problem associated with (5) allows estimation of the numerical eigenfrequencies computed with the finite-difference scheme. As usual with finite differences, a fine grid is necessary in order to have significant accuracy in the computed frequencies, and the accuracy

| | | | | | | | | |
|---|---|---|---|---|---|---|---|---|
| 21.65 | 41.63 | 66.61 | 74.93 | 86.59 | 119.89 | 121.55 | 141.54 | 161.52 |
| 166.52 | 181.50 | 194.82 | 226.46 | 241.44 | 246.44 | 254.76 | 266.42 | 299.72 |
| 299.72 | 301.39 | 341.35 | 346.35 | 374.65 | 381.32 | 386.31 | 401.29 | 406.29 |

Table 1: Eigenfrequencies (analytical values, in Hz) of the selected plate for the simulations, $L_x = 0.4$m, $L_y = 0.6$m, $h$=1 mm, $E$= 200 GPa, $\nu$=0.3 and $\rho$=7860 kg.m$^{-3}$.

decreases with mode number. It is worth noting, however, that accuracy is rather good over the entire spectrum, up to the Nyquist frequency—such is not the case, for example, for Chebyshev spectral methods, which compute low modes with very high accuracy, but fail spectacularly in computing high frequency modal frequencies. Because the interest here is in obtaining wide band responses at a reasonable sample rate, simpler finite difference schemes are a good alternative. Figure 2 and Table 2 illustrate the numerical accuracy obtained. In Figure 2, the relative deviation of the computed eigenfrequencies with respect to the analytical values are shown by plotting:

$$\Delta_f^i = \frac{|\omega_i^{f_S} - \omega_i^a|}{\omega_i^a}, \tag{20}$$

where $\omega_i^{f_S}$ stands for the numerical i$^{th}$ eigenfrequency, computed with the given sampling rate $f_S$, and $\omega_i^a$ is the analytical i$^{th}$ eigenfrequency recalled in Eq. (19), in the frequency range [0, 5000] Hz. One can see that for $f_S$=100 000 Hz, the relative deviation of the eigenfrequencies is less than 10% up to 5000 Hz, *i.e.* until the 370$^{th}$ mode.

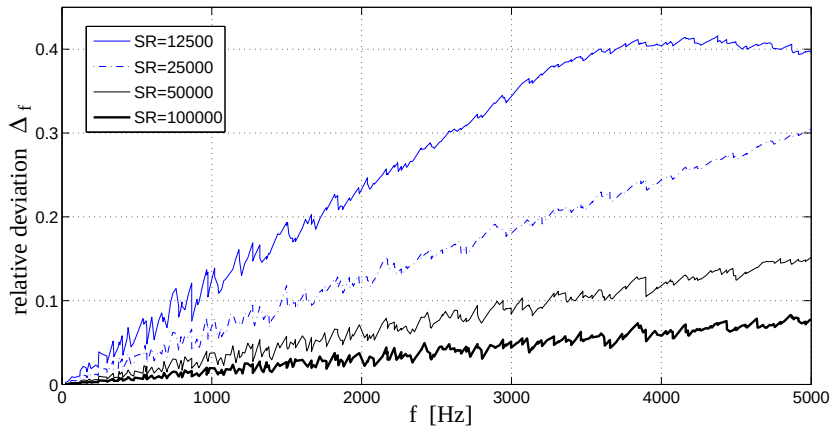


Figure 2: Relative deviation $\Delta_f^i$ between analytical eigenfrequencies of a simply supported plate and those computed with the finite difference scheme with increasing $f_S$, in the frequency range [0, 5000] Hz.

Recalling that our interest is matching the experimental observations discussed in the introduction, the frequency range of interest for the choice of the forcing frequency will not exceed 400 Hz, as it allows simulation of the transition scenario up to the 30$^{th}$ mode, hence giving rise to numerous bifurcations. In the experiments, the same frequency range was also tested, mainly because the amplitude of forces required to attain the turbulent regime for higher excitation frequencies is generally out of range for conventional shakers. Table 2 shows, for the computed eigenfrequencies shown in Figure 2, the number of grid points used, as well as the maximal

| $f_S$ Sampling rate (Hz) | $N_x$ | $N_y$ | $(N_x-1)(N_y-1)$ Number of grid points | [0,500] Hz *up to 34$^{th}$ mode* | [0,2000] Hz *up to 144$^{th}$ mode* | [0,5000] Hz *up to 370$^{th}$ mode* | [0,10000] Hz *up to 755$^{th}$ mode* |
|---|---|---|---|---|---|---|---|
| 12500 | 18 | 27 | 442 | 6.8% | 23.5% | 41.6% | / |
| 25000 | 25 | 37 | 864 | 3.6% | 13.0% | 30.4% | 41.6% |
| 50000 | 36 | 54 | 1855 | 1.7% | 7.1% | 15.1% | 28.9% |
| 100000 | 51 | 76 | 3750 | 0.9% | 3.7% | 8.3% | 15.2% |

Table 2: Convergence of numerical eigenfrequencies on selected frequency bands. For each value of $f_S$, the number of grid points used in the scheme is given, as well as the maximum deviation $\Delta_f^i$ on four frequency intervals.

deviations within some selected frequency ranges. One can conclude that a fair accuracy is obtained for the eigenfrequencies up to 500 Hz for $f_S$=25000 Hz, hence allowing the simulation of the transition to turbulence for the first 30 eigenfrequencies. Obtaining better accuracy for larger frequency bands requires a number of points for simulation which increases rapidly. As compared to a preceding study on the transition to chaotic vibrations in circular plates where a Galerkin modal projection was used to discretize the equations [25], one can conclude that with the present method, a very large number of modes is retained in the simulation. However their accuracy is limited although the lower modes are finely represented. Convergence will be further studied in the next section in order to select an operational value for the simulations.

### *3.2. Conservation of energy and nonlinear convergence*

For the dimensional problem defined by Eqs (2) and without imperfection ($w_0 = 0$ gives a perfect plate), one can define the kinetic energy $\bar{T}$, the bending $\bar{V}$ and the in-plane energy $\bar{U}$ as [38, 16]:

$$\bar{T} = \int\int_{\bar{\mathcal{S}}} \frac{\rho h}{2} \dot{\bar{w}}^2 \mathrm{d}\bar{\mathcal{S}}, \tag{21a}$$

$$\bar{V} = \int\int_{\bar{\mathcal{S}}} \frac{D}{2} (\Delta \bar{w})^2 \mathrm{d}\bar{\mathcal{S}}, \tag{21b}$$

$$\bar{U} = \int\int_{\bar{\mathcal{S}}} \frac{1}{2Eh} (\Delta \bar{F})^2 \mathrm{d}\bar{\mathcal{S}}, \tag{21c}$$

where $\bar{\mathcal{S}} = [0, L_x] \times [0, L_y]$ is the dimensional area of the plate. When undamped vibrations are considered ($\bar{\sigma}_0 = 0$) and for conservative boundary conditions (such as those of simply-supported type), the total energy of the plate (or Hamiltonian) $\bar{H} = \bar{T} + \bar{V} + \bar{U}$ is conserved during any motion. Note the simplified form for the bending energy (21b), arising from the fact that simply-supported boundary conditions are considered [38, 16].

After the scaling defined in Eqs (4), one obtains the following form for the scaled energies:

$$\bar{T} = \frac{\rho h^3 L_x L_y}{6(1-\nu^2)} T, \quad \text{with} \quad T = \int\int_{\mathcal{S}} \frac{1}{2} \dot{w}^2 \mathrm{d}\mathcal{S}, \tag{22a}$$

$$\bar{V} = \frac{\rho h^3 L_x L_y}{6(1-\nu^2)} V, \quad \text{with} \quad V = \kappa^2 \int\int_{\mathcal{S}} \frac{1}{2} (\Delta w)^2 \mathrm{d}\mathcal{S}, \tag{22b}$$

$$\bar{U} = \frac{\rho h^3 L_x L_y}{6(1-\nu^2)} U, \quad \text{with} \quad U = \kappa^2 \int\int_{\mathcal{S}} \frac{1}{2} (\Delta F)^2 \mathrm{d}\mathcal{S}, \tag{22c}$$

with $\mathcal{S}$=[0, $\sqrt{L_x/L_y}$]×[0, $\sqrt{L_y/L_x}$] the scaled area. The discrete counterparts of the scaled forms of the energies $T$, $U$ and $V$ are defined through:

$$\mathfrak{t} = \frac{1}{2}\|\delta_{t^-} w\|_{\mathfrak{s}}^2, \tag{23a}$$

$$\mathfrak{v} = \frac{1}{2}\kappa^2 < \delta_\Delta w, e_{t^-}\delta_\Delta w >_{\mathfrak{s}}, \tag{23b}$$

$$\mathfrak{u} = \frac{1}{2}\kappa^2 \mu_{t^-} \|\delta_\Delta F\|_{\mathfrak{s}}^2, \tag{23c}$$

where the scalar product $< f, g >_{\mathfrak{s}}$ between two discrete functions $f \equiv f_{l,m}$ and $g \equiv g_{l,m}$ defined on the discrete domain $\mathfrak{s} = [0, N_x] \times [0, N_y]$ is given by:

$$< f, g >_{\mathfrak{s}} = h_x h_y \sum_{l=0}^{N_x} \sum_{m=0}^{N_y} f_{l,m} g_{l,m} \tag{24}$$

In Eqs (23), the expression for $\mathfrak{u}$ is simplified to the specific scheme selected with $\gamma$=1 and $\beta$=0. These expressions are constructed so as to obtain the conservation of the total energy or discrete Hamiltonian of the system. For $\sigma_0 = 0$ and conservative boundary conditions, the conservation relationship $\delta_{t^+}\mathfrak{h} = 0$ with $\mathfrak{h} = \mathfrak{t} + \mathfrak{v} + \mathfrak{u}$ is demonstrated in [32].

Figure 3 shows a typical simulation with the selected plate, excited with a frequency of 87 Hz (in the vicinity of the fifth eigenfrequency), where the amplitude of the forcing is first increased from 0 to 30 N in 7 seconds, then kept constant during 7 seconds, and finally set to zero in the remaining 7 seconds of the simulation. An undamped plate is considered in this simulation ($\sigma_0 = 0$) in order to numerically verify the conservation of energy. An arbitrary output point from the plate is selected for analyzing the vibration. It is located at $\overline{x} = 0.2L_x$, $\overline{y} = 0.3L_y$, and will be denoted by $w^{out}$ in the remainder of the article. The spectrogram of $w^{out}$ shows a transition from periodic to turbulent behaviour occurring at $t$=5 s. As no damping is considered, the turbulent state persists once the external forcing is set to zero. Figure 3(c) shows the behaviour of the computed energies during the simulation: the total energy $\mathfrak{h}$ being decomposed between its transverse $\mathfrak{t} + \mathfrak{v}$ and in-plane $\mathfrak{u}$ components. As long as the forcing is not cancelled, energy is fed to the plate that can not be dissipated, hence the total energy of the system increases continuously. Once the forcing set to zero, a perfect conservation of energy (to machine accuracy) is found. A significant increase of the in-plane energy is observed during the turbulent behaviour. This peculiar feature will be discussed in section 5 where will we show that it results from the relaxation of the simulated system to an absolute equilibrium state that has no physical meaning, and is only a consequence of the truncation imposed by the numerics. The simulation shown in Fig. 3 has been computed with $f_S$=50 kHz and lasts 18 hours on a standard PC with a CPU clock at 2 GHz.

The same simulation is shown in Fig. 4, where a linear viscous damping term has been added to the dynamics. The damping value has been set to $\sigma_0 = 0.75$, consistent with what is observed in metallic plates, as well as what was chosen in [25]. In Fig. 4, the decay time is around 7 seconds which corresponds to what is usually measured. This value, $\sigma_0 = 0.75$, will be kept in the remainder of the study.

The same excitation frequency has been chosen, so that a direct transition is still observed, as no internal resonance relationships are fulfilled for this excitation frequency. As compared to the undamped case where energy is present in the whole spectrum, up to $f_S/2$, the damping limits the frequency span of the turbulent regime by adding a dissipative scale to the system.

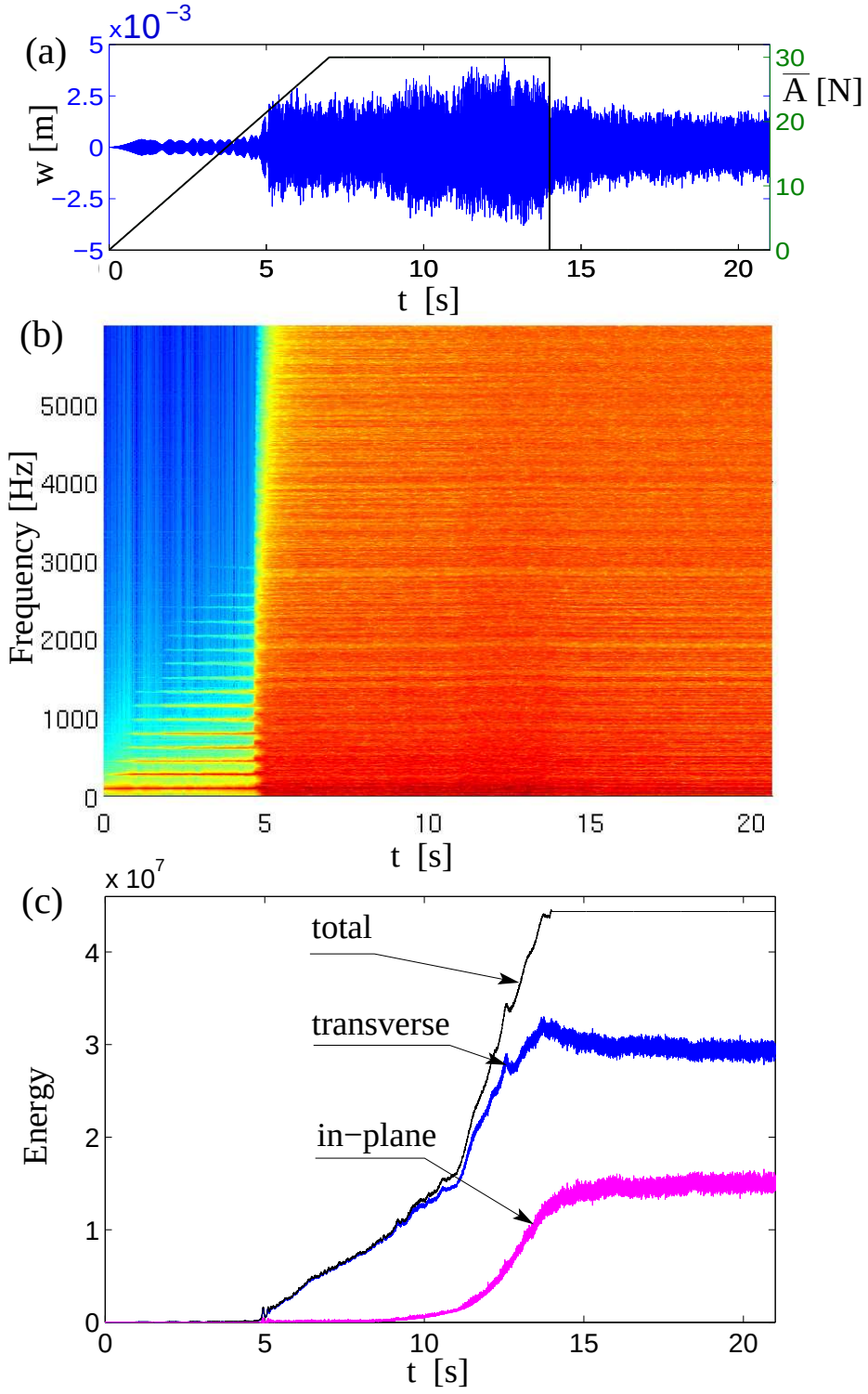


Figure 3: Transverse vibration and energy of an undamped plate excited at 87 Hz. (a): transverse displacement $w^{out}$ at one point on the plate and history of the dimensioned loading amplitude $A$ on the right axis. (b): Spectrogram of $w^{out}$. (c): Total discrete energy (arbitrary units) $\mathfrak{h}$ (black) of the plate during the simulation, decomposed into its bending (transverse) component $\mathfrak{t} + \mathfrak{v}$ (blue) and its in-plane component $\mathfrak{u}$ (magenta).

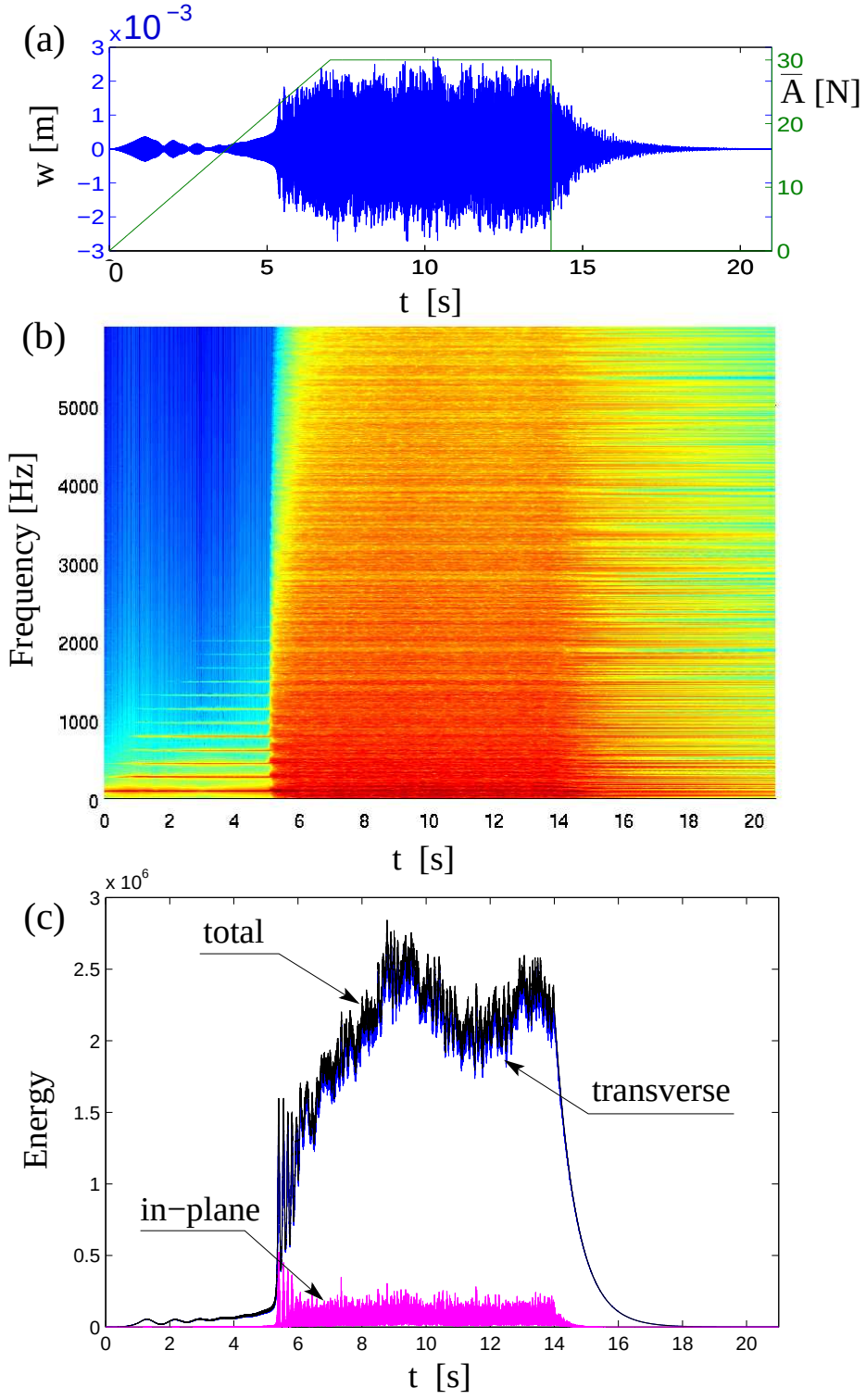


Figure 4: Transverse vibration and energy of the damped plate ($\sigma_0$=0.75) excited at 87 Hz. (a): output transverse displacement $w^{out}$ and history of the loading amplitude $A$. (b): Spectrogram of $w^{out}$. (c): Total discrete energy ɧ (black) of the plate during the simulation: transverse component ŧ + ʊ (blue) and in-plane component ʉ (magenta).

Here, energy is present up to 10 kHz. The energetic behaviour shows that in-plane energy $\mathfrak{u}$ remains limited to very small values so that transverse energy $\mathfrak{t} + \mathfrak{v}$ is almost superposed to $\mathfrak{h}$.

| $f^{exc}$ (Hz) \ $f_S$ (kHz) | 2.5 | 5 | 10 | 15 | 25 | 35 | 50 | 75 |
|---|---|---|---|---|---|---|---|---|
| 22 Hz | 5.8 | 10.1 | 7.1 | 14.4 | 15.8 | 15.8 | 15.8 | / |
| 75 Hz | 3.4 | 6.1 | 7.1 | 11.8 | 10.1 | 10.1 | 10.1 | / |
| 227 Hz | 4.9 | 8.6 | 13.1 | 18.1 | 18.9 | 18.9 | 20.1 | 20.1 |

Table 3: Critical value $\bar{A}_{cr}$ (in N) of the amplitude of the external forcing for which the turbulent behaviour sets in, as a function of the sampling frequency $f_S$ in kHz (first row), and for three different excitation frequencies $f^{exc} = \Omega/2\pi$: 22 Hz, 75 Hz and 227 Hz.

In order to gain some insight into (and confidence in) the convergence of the numerical results with respect to the chosen sampling rate $f_S$ and consequently the number of grid points used to simulate the plate dynamics, a convergence study with respect to the critical force needed to attain the turbulent behaviour is conducted, in the same manner as in [25]. More specifically, in order to obtain the long-term behaviour of the plate for a given forcing amplitude, instead of continuously increasing $A$, the variation interval $[0, A_{max}]$ is separated into 50 steps, and A is incremented by small steps (around 0.5 N) and a constant value is maintained on each subinterval. The length of each subinterval is 350 periods so that the transient behaviour can be fully damped, and after that 60 periods of the vibration response are recorded for analyzing the behaviour (periodic, quasi-periodic or turbulent). This kind of numerical simulation strictly follows the *modus operandi* presented in [25] for circular plates. This results in extremely long simulations that lasts around 3 weeks for each of the three forcing frequencies tested. Table 3 shows the obtained results for increasing values of $f_S$, where the critical force $\bar{A}_{cr}$ (in N), where the turbulent behaviour sets in, is reported. For $f_S$=35 kHz, the critical forcing amplitude obtained is converged. This observation recovers results already shown [25] explaining that this critical forcing value appears to be controlled by the low-frequency part of the dynamics (slow-flow equations), so that a very refined grid is not necessary for obtaining convergence in the first regime. This will not be the case anymore for the turbulent regime where higher values of $f_S$ are needed due to the presence of the energy flux through lengthscales. this will be discussed in section 5. For studying the transition scenario, the sampling frequency has been selected as $f_S = 50$ kHz.

In order to get a complete picture of the transition scenario, 33 simulations have been realized for frequencies in the range [20, 350] Hz. Within this frequency range, 21 modes are present. 21 simulations have thus been realized around the eigenfrequencies, from 22 Hz for the first to 342 Hz for the $21^{th}$, and 12 additional frequencies have been tested to observe the scenario away from linear resonances. The results are divided in two frequency bands, "low frequency" from the fundamental to the ninth mode at 162 Hz, and "high frequency" from 167 Hz to 342 Hz. This distinction is made with regard to the obtained results. As will be shown subsequently, in the low frequency range, the generic transition scenario observed is that of a direct transition to turbulence, whereas in the "high frequency" range, the most common encountered case was that of a three-stage scenario with the appearance of the quasiperiodic regime before the turbulent state.

### *3.3. Low frequency excitation*

#### *3.3.1. Generic case*

In the low frequency range, 17 frequencies have been tested. They are given as follows, in parenthesis is indicated the critical value $\bar{A}_{cr}$ (in N) for which the turbulent behaviour sets in: 22 Hz (22 N), 42 Hz (56 N), 65 Hz (51 N), 67 Hz (38 N), 70 Hz (18 N), 75 Hz (16 N), 80 Hz (15 N), 87 Hz (21 N), 118 Hz (56 N), 120 Hz (54 N), 122 Hz (55 N), 125 Hz (52 N), 127 Hz (25 N), 130 Hz (18 N), 131 Hz (20 N), 142 Hz (15 N) and 154 Hz (45 N). Note that the critical force amplitude $\bar{A}_{cr}$ is given in an indicative manner, and the values can be slighlty different from those reported in Table 3.2 as in these experiments the forcing amplitude was linearly increased in 20 seconds without waiting for the transient to die away at each force step. A more thorough study of the critical force is reported in [25] for circular plates.

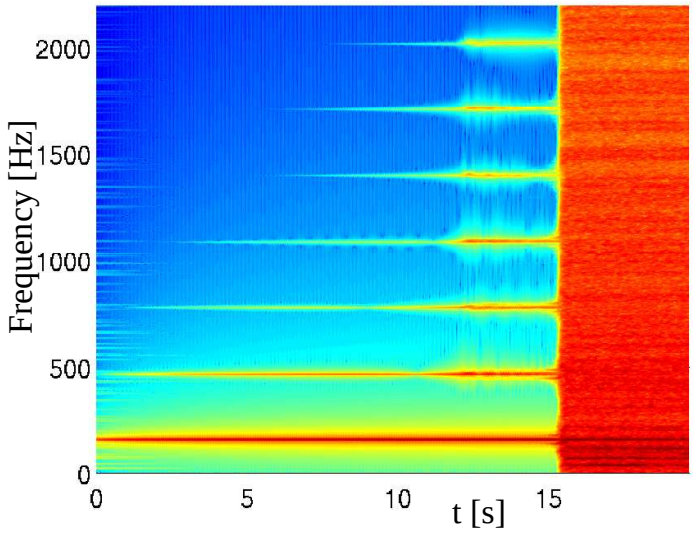


Figure 5: Spectrogram of output displacement $w^{out}$ for the plate excited at 154 Hz, with a linearly increasing force from 0 to 60 N over 20 seconds. A direct transition to turbulence is observed, occurring at t=15 s, *i.e.* for F=45 N.

Figure 5, where the plate is excited at 154 Hz, shows the generic case observed in the low frequency range: a direct transition to turbulence, as is also the case presented in Fig. 4 with $f^{exc}$=87 Hz. In both cases, a first regime is obtained where the directly excited mode vibrates nonlinearly, hence creating odd harmonics of the excitation frequency that are clearly present. As expected from perfect non-linear plate dynamics containing only a cubic nonlinearity due to the internal force symmetry with respect to the middle surface, no even harmonics are present in the response. In Fig. 4 with $f^{exc}$=87 Hz, *i.e.* in the vicinity of the fifth mode, the turbulent behaviour suddenly settles down for $F$=21 N, whereas this critical amplitude needs to be attained at 45 N for $f^{exc}$=154 Hz, mainly because 154 Hz is not in the vicinity of an eigenfrequency so that a higher amplitude is needed to attain large amplitudes of vibrations (linear resonance). The direct transition has been observed for all the frequencies tested in the low-frequency range, namely for : 22 Hz, 42 Hz, 70 Hz, 80 Hz, 87 Hz, 118 Hz, 120 Hz, 122 Hz, 125 Hz, 131 Hz and 154 Hz. This generic behaviour is interpreted as a reflection of the fact that no internal resonance relationships exist between the very low-order eigenfrequencies that are excited here. Hence the energy is stored in an eigenmode motion which cannot exchange its

energy with other internally resonant modes, until the stability limit is attained and the turbulent regime sets in. As the direct transition do not need specific investigations, we turn now to the analysis of the particular cases obtained for some frequencies in the low-frequency range.

### *3.3.2. Particular cases*

The six remaining frequencies show a different transition scenario, three of them being illustrated in Figs 6, 7 and 8.

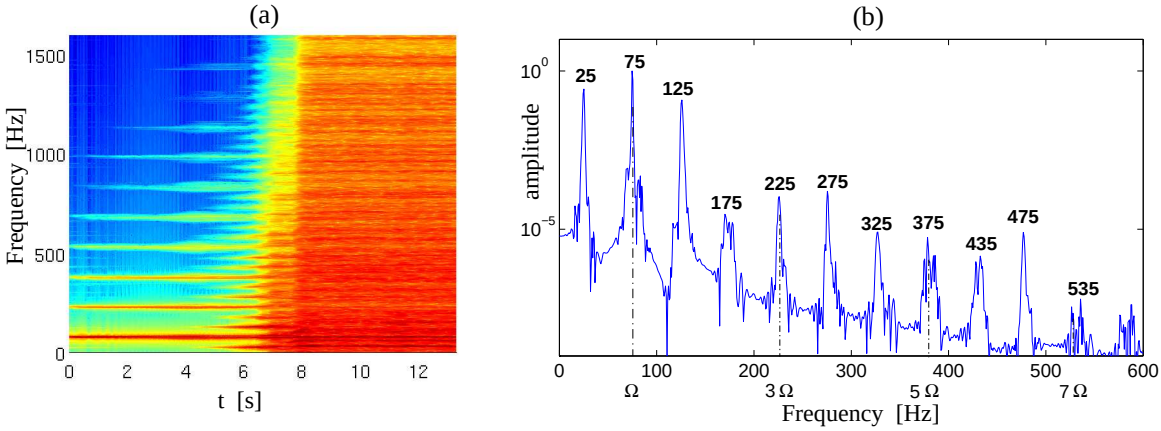


Figure 6: (a): Spectrogram of output displacement $w^{out}$ for the plate excited at 75 Hz, with a forcing amplitude $F$ from 0 to 28 N in 14 seconds. A superharmonic resonance is excited with participation of the first mode locked at 25 Hz from t=5 s, then the turbulent regime is obtained at t=8 s, *i.e.* for F=16 N. (b): Fourier transform of a 1.3 sec (Hanning window of $2^{16}$=65536 points) computed at $t$=6 s showing the spectral content of the vibration in the coupled superharmonic regime.

The first particular case studied is represented in Figure 6, observed for $f^{exc}$=75 Hz, *i.e.* in the vicinity of the fourth mode of the plate. The amplitude of the forcing is increased linearly from 0 to 28 N in 14 seconds. The first regime is the moderately non-linear regime where only the directly excited mode participates in the plate response. At $t$=5 s, a bifurcation is observed with the clear appearance of a frequency of 25 Hz in the vibration, as highlighted in Fig. 6(b). This frequency peak is the signature of the first eigenmode participation through a superharmonic 1:3 resonance. It occurs for a non-negligible forcing amplitude (10 N), mainly because the 1:3 resonance relationship is not perfectly satisfied. Hence the 1:3 resonance relationship can be satisfied only for an energy that is sufficient so as to obtain a frequency shift of the first mode. The fact that internal resonance can occur between modes that are not commensurate natural frequencies has already been observed in [46, 47, 48, 49]. When increasing amplitudes of vibrations and thus the total energy level, periodic solutions follow nonlinear normal mode (NNM) branches, showing large variations of frequencies. Thus internal resonances can be fulfilled between the shifted frequencies, so that the examination of natural frequencies to predict possible mode coupling is not enough. A correct representation is to compute the variations of all eigenfrequencies as a function of the total energy of the system, resulting in a so-called Frequency-Energy Plot (FEP) [50]. The numerical result obtained here for $f^{exc}$=75 Hz seems to verify this kind of behaviour and resembles the results shown in [48] on a simple two degrees-of-freedom (dofs) system. This assumption could be fully confirmed by computing the complete FEP of the plate for the first frequencies, which is out of the scope of the present study. Once activation of the 1:3 superharmonic resonance is realized, the spectrum, shown in Fig. 6(b), is

logically composed of peaks being separated by 75-25= 50 Hz. However, one can observe that the third peak at 125 Hz is proeminent as compared to the followings, as it has almost equal energy than the spectral component at 25 Hz. As the seventh mode of the plate is given at 121.5 Hz, a possible assumption here is that this mode is also excited via energy transfer so that a 3-modes dynamics is present after the first bifurcation. The coupled regime persists during 4 seconds and is enriched in spectral content with an increase of the width of the spectral peaks, until the turbulent regime sets in for a forcing amplitude of $F$=16 N.

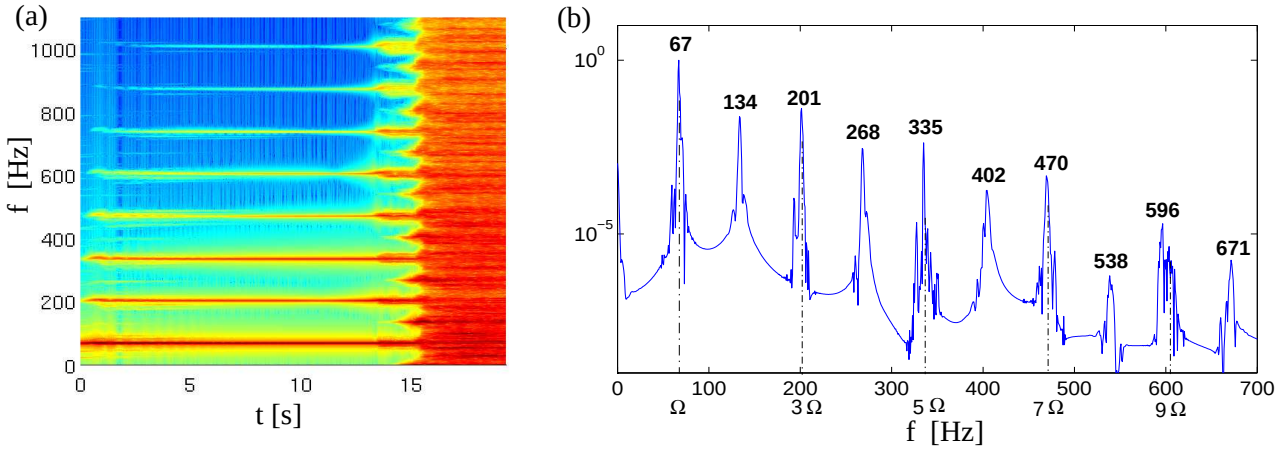


Figure 7: (a): Spectrogram of output vibration $w^{out}$ for the plate excited at 67 Hz, with a forcing amplitude $F$ from 0 to 50 N in 20 seconds. A symmetry-breaking (SB) bifurcation is observed with the appearance of even harmonics in the response, before the turbulent regime. (b): Fourier transform of a 1.3 sec segment (Hanning window of $2^{16}$=65536 points) computed at $t$=14.5 s showing the spectral content of the vibration after the SB bifurcation.

Surprisingly enough, the 1:3 superharmonic resonance has not been observed in the vicinity of the third mode, the eigenfrequency of which more closely fulfills the 1:3 ratio needed. This is confirmed in Fig. 7 where the scenario for $f^{exc}$=67 Hz is shown. For this frequency, the 1:3 resonance is not excited, and a symmetry-breaking (SB) bifurcation is observed, which is characterized by the appearance of even harmonics in the response before the turbulent regime and a wideband Fourier spectrum. The SB bifurcation is classically observed in the Duffing equation, its location in the plane being, in frequency, between the 1:3 superharmonic and the main resonance; see *e.g.* [51, 52]. It has also been observed in the FEP of the two dofs system analyzed in [48, 49], where it was found to appear before the 1:3 internal resonance, what also seems to be observed here in the case of the plate. Once again, a complete picture of the internal resonance must include the energy level, so that a FEP should fully confirm the assumptions for the mode coupling observed here for $f^{exc}$=75 Hz and $f^{exc}$=67 Hz.

Finally, two other numerical experiments have been conducted in this frequency range, $f^{exc}$=65 Hz and 70 Hz. For $f^{exc}$=65 Hz, neither the SB bifurcation is found, nor the superharmonic resonance. Instead, a short quasiperiodic regime sets in with a clear appearance of frequency peaks at 25 Hz, 105 Hz and 155 Hz between the excitation frequency and the third harmonic at 195 Hz. These five frequencies fulfill third-order relationships so that an energy transfer is at hand. However, apart from the first frequency at 25 Hz that can be easily related to the first mode, it appears to be more difficult to relate the two new frequencies at 105 and 155 Hz to an eigenfrequency. Noting that the first regime is destabilized at a high value of

the forcing (around 50 N) for $f^{exc}$=65 Hz, one can conclude that the frequencies have already encountered a large variation due to nonlinearity. In the last test with $f^{exc}$=70 Hz, a direct transition is obtained, highlighting that the internal resonance relationships exist on narrow frequency intervals.

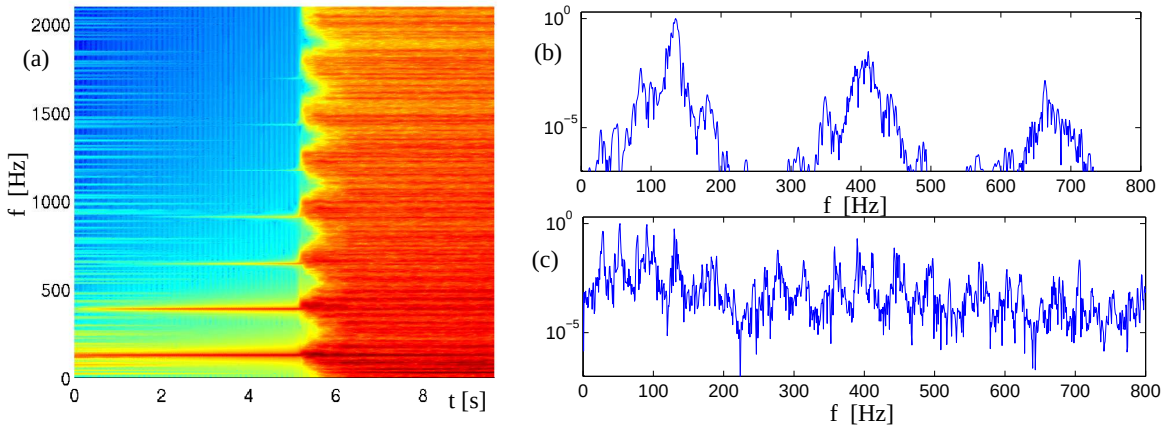


Figure 8: (a): Spectrogram of the output vibration $w^{out}$ for the plate excited at 130 Hz, with a forcing amplitude $F$ from 0 to 30 N in 10 seconds. A direct transition is observed with frequency peaks of increasing width just before the turbulent regime. (b) and (c) : Fourier transforms of a 1.3 sec segment computed respectively at $t$=5 s and $t$=8 s.

The last case shown for the low frequency range is represented in Fig. 8, for $f^{exc}$=130 Hz. A similar behaviour has also been found for $f^{exc}$=127 Hz and 142 Hz. Here the peculiar feature is a marked broadening of the spectral peaks around all harmonics just before the turbulent regime, as illustrated in the two spectra of the output displacement $w^{out}$ shown in Fig. 8(b-c). The interpretation of this bifurcation is not straightforward in this case, as it appears slightly different from a direct transition, but it could also be seen as a quasiperiodic state involving so many modes that peak identification is difficult. We note also that this spectral enlargement is one of the characteristics of modulation instability [53, 54, 55], which could be the correct interpretation in these cases. It is worth noting that these kinds of transitions have also been observed experimentally. Further research specifically concentrated on this case is however needed to ensure the category in which it falls. In the remainder of the article, this type of scenario will be called, for lack of a better term, modulation instability; at this stage it is simply a blanket term for a phenomenon that needs a more complete characterization.

### *3.4. High frequency excitation*

In this section we discuss the results obtained in the frequency range [167, 342] Hz, here called the ”high frequency range” because the observed scenario differs radically from the cases discussed in the previous section. 15 numerical experiments have been conducted, and only two direct transitions without quasiperiodic regime have been found, whereas ten cases of energy transfer within the quasiperiodic regime have been observed, and three cases corresponding to the more difficult case shown previously with $f^{exc}$=130 Hz and called modulation instability. The tested frequencies are (in parenthesis the case obeserved: D for direct transition, QP for quasiperiodic regime, MI for Modulation instability, as well as the critical force amplitude $\bar{A}_{cr}$ (in N) for which the turbulent behaviour sets in): 167 Hz (QP, 58 N), 171 Hz (MI, 30 N), 182 Hz

(QP, 31 N), 184 Hz (QP, 37 N), 190 Hz (QP, 21 N), 195 Hz (QP, 24 N), 198 Hz (QP, 66 N), 202 Hz (D, 19 N), 227 Hz (MI, 82 N), 230 Hz (QP, 100 N), 247 Hz (MI, 18 N), 300 Hz (QP, 42 N), 302 Hz (QP, 40 N), 304 Hz (QP, 20 N), 342 Hz (D, 50 N). Hence the dominant observed scenario is that of the appearance of the quasiperiodic regime, which will now be further highlighted. It is explained by the fact that exciting the plate at a higher frequency with numerous eigenmodes before the excitation frequency renders possible a larger number of resonance relationships, hence making this scenario more likely to appear. Three cases are shown and discussed.

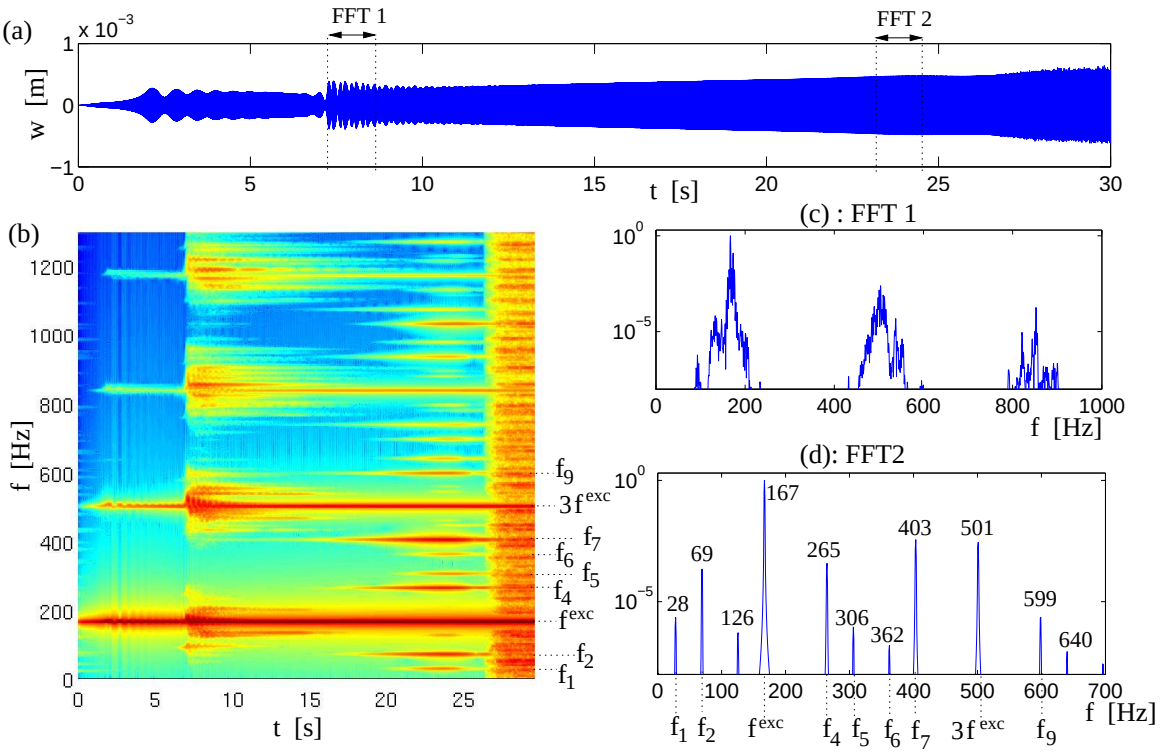


Figure 9: Transition scenario to turbulence for the perfect plate excited at 167 Hz, with a forcing amplitude from 0 to 65 N in 30 seconds. (a) : time series of the output displacement $w^{out}$. (b) : spectrogram of the vibration. (c) and (d) : Fourier transforms of 1.3 s of the displacement, respectively at t=7.5 s (c), and t=23 s (d).

The first case is that of the excitation frequency $f^{exc}$=167 Hz, in the vicinity of the tenth mode, depicted in Fig. 9, where the amplitude of the forcing $\bar{A}$ is increased from 0 to 65 N in 30 seconds. A first bifurcation is observed at $t$=7.5 s, leading to a transient regime that fail to stabilize and lasts 5 seconds. This unstable transient regime is characterized by an increased width of the spectral peaks of the forcing harmonics, as shown in the first spectrum in Fig. 9(c). Then the stable quasiperiodic regime sets in, with a clear appearance of distinct frequency peaks shown in Fig. 9(d). For a better identification, the most prominent frequency peaks are denoted as: $f_1$ = 28 Hz, $f_2$ = 69 Hz, $f_3$ = $f^{exc}$ = 167 Hz, $f_4$ = 265 Hz, $f_5$ = 306 Hz, $f_6$ = 362 Hz, $f_7$ = 403 Hz, $f_8$ = $3f^{exc}$ = 501 Hz and $f_9$ = 599 Hz. All of these new frequencies share evident order-three internal resonances amongst themselves, highlighting the fact that energy has been transferred in order to arrive at the quasiperiodic regime. For most of them, they can also be easily identified to eigenfrequencies of the plate. From the order of appearance and respective magnitude of these peaks, the following scenarios can be identified. The first frequencies to appear, $f_2$, $f_4$, $f_7$ and $f_9$ are related to the excitation frequency $f_3$ = $f^{exc}$ by the following

relationships:

$$f_3 = f_7 - f_2 - f_3, \tag{25a}$$
$$f_3 = f_9 - f_4 - f_3. \tag{25b}$$

Moreover, $f_2$, $f_4$, $f_7$ and $f_9$ are near eigenfrequencies, respectively to modes number 3, 17, 26 and 41. Hence a first double order-three internal resonance is excited leading to a quasiperiodic regime with 5 modes exchanging energy. This 5-modes dynamics is rapidly destabilized for a more complicated regime including more modes, corresponding to all the frequency peaks identified in Fig. 9. These new frequencies appear with a little delay as compared to the first four identified, but they also share evident order-three relationships:

$$f_3 = f_4 + f_7 - f_8, \tag{26a}$$
$$f_3 = f_6 + f_5 - f_8, \tag{26b}$$
$$f_3 = f_1 + f_8 - f_6. \tag{26c}$$

Eventually, the quasiperiodic regime involves 9 modes excited through energy transfers. The last bifurcation involves destabilization of this complicated 9-modes dynamics in favour of the turbulent regime.

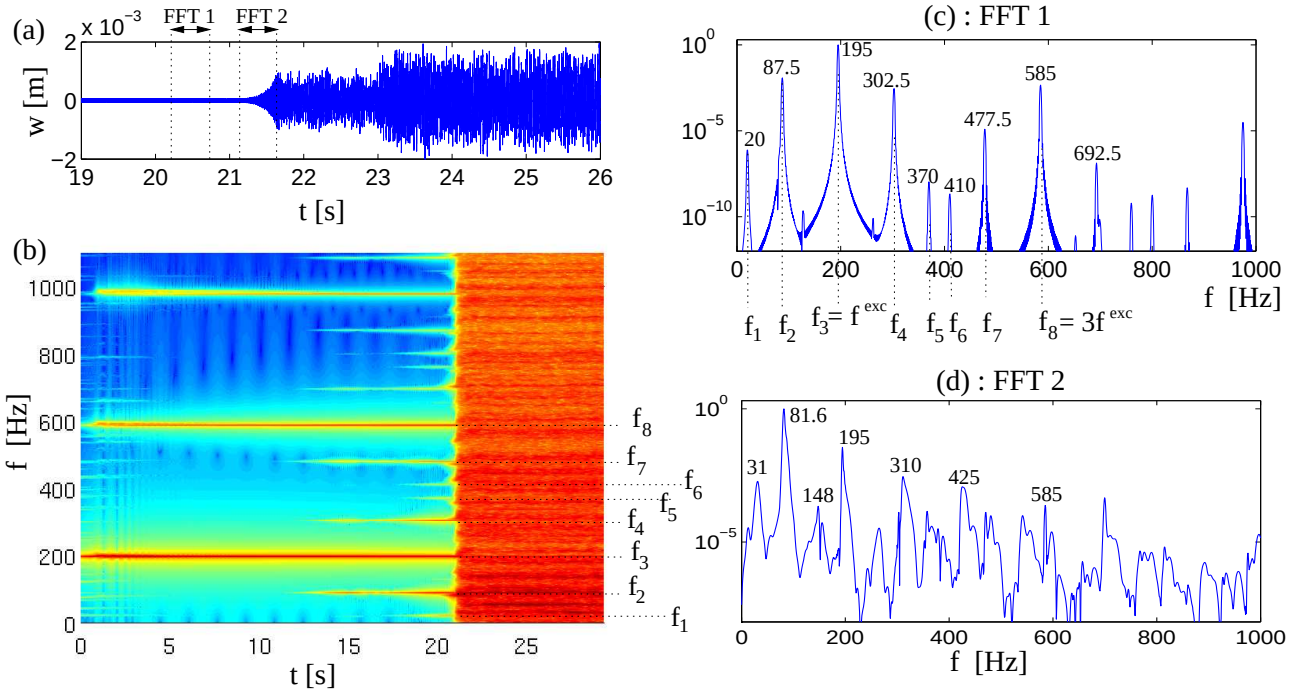


Figure 10: Transition scenario to turbulence for the perfect plate excited at 195 Hz, with a forcing amplitude from 0 to 35 N in 30 seconds. (a) : time series of the output displacement $w^{out}$, zoom on the transition between 19 and 26 s. (b) : spectrogram of the vibration. (c) and (d) : Fourier transforms of 0.65 s of the displacement, respectively at t=20 s (c), and t=21.1 s (d).

The second case selected for analysis is shown in Fig. 10, and corresponds to an excitation frequency of $f^{exc}$= 195 Hz, in the vicinity of the $12^{\text{th}}$ eigenfrequency. The forcing amplitude is increased from 0 to 35 N in 30 seconds in this numerical experiment. The spectrogram, in

Fig. 10(b), shows a clear scenario with a quasiperiodic state before the turbulent regime. The quasiperiodic state sets in progressively with the appearance of the following frequency peaks, identified in Fig. 10(b-c) : $f_1 = 20$ Hz, $f_2 = 87.5$ Hz, $f_3 = f^{exc} = 195$ Hz, $f_4 = 302.5$ Hz, $f_5 = 370$ Hz, $f_6 = 410$ Hz, $f_7 = 477.5$ Hz, $f_8 = 3f^{exc} = 585$ Hz. The first step involves energy transfers between $f_2$ (in the vicinity of mode 5), $f_4$ (mode 20), $f_7$ (mode 32). The energy, injected on $f_3 = f^{exc} = 195$ Hz spread to these new frequency peaks appearing first in the spectrogram through the following order-three internal resonance relationships:

$$2f_3 = f_2 + f_4 = f_7 - f_2. \tag{27}$$

Then, as shown in the displacement spectrum in Fig. 10(c), a new set of frequencies is excited through new internal resonance relationships. They appear later in the spectrogram with a smaller amplitude, indicating that the first identified resonance dominates. These new peaks, $f_1$, $f_5$ and $f_6$ are not directly related to the excitation frequency $f_3 = f^{exc}$ or its third harmonics, so that their appearance is conditioned by the fact that the first step has been excited and that energy is present in $f_2$, $f_4$ and/or $f_7$. This second instability is characterized by energy transfers through the following identified relationships:

$$f_3 = f_1 + 2f_2, \tag{28a}$$
$$f_4 = f_1 + f_2 + f_3, \tag{28b}$$
$$f_5 = f_4 + f_2 - f_1, \tag{28c}$$
$$f_6 = f_4 + f_2 + f_1, \tag{28d}$$
$$f_7 = f_2 + f_1 + f_5. \tag{28e}$$

After this second instability, the quasiperiodic regime involves 8 modes. It is quickly destabilized in favour of the turbulent regime which sets in rapidly. Interestingly, once the turbulent regime is attained, energy is redistributed through all the lengthscales, so that the most prominent peaks, identified in Fig. 10(d), are distinct from the ones identified in the quasiperiodic regime, where the frequencies were locked to fulfill internal resonance relationships.

The last case analyzed is shown in Fig. 11, for $f^{exc}$= 230 Hz, with a forcing amplitude increasing from 0 to 110 N in 20 seconds. Once again a clear quasiperiodic regime sets in before the turbulent behaviour, hence recovering the general transition scenario inferred from the experimental measurements. The quasiperiodic state is much more complicated in this case with the appearance of 5 frequencies under the excitation frequency. All the frequency peaks share order-three internal resonance relationships, and there is a gap of 40 Hz between the majority of them.

Finally, all other excitation frequencies tested in this "high frequency" range show a similar behaviour to that observed in the three cases illustrated. Consequently the generic transition scenario is fully confirmed by these numerical experiments. We now turn to an imperfect plate to simulate a more realistic case, because in experiments imperfections are unavoidable and order-two internal resonances in the quasiperiodic regime are always observed.

## 4. Simulation results for the imperfect plate

### *4.1. Selected case*

The case of an imperfect plate is now studied by imposing a static deflection $w_0(x, y)$ to the mid-plane of the plate having the form of a raised cosine:

$$w_0(x, y) = \frac{1}{2} A_{imp} \left[ 1 + \cos\left( \frac{\pi \sqrt{(x - x_0)^2 + (y - y_0)^2}}{L_{imp}} \right) \right]; \tag{29}$$

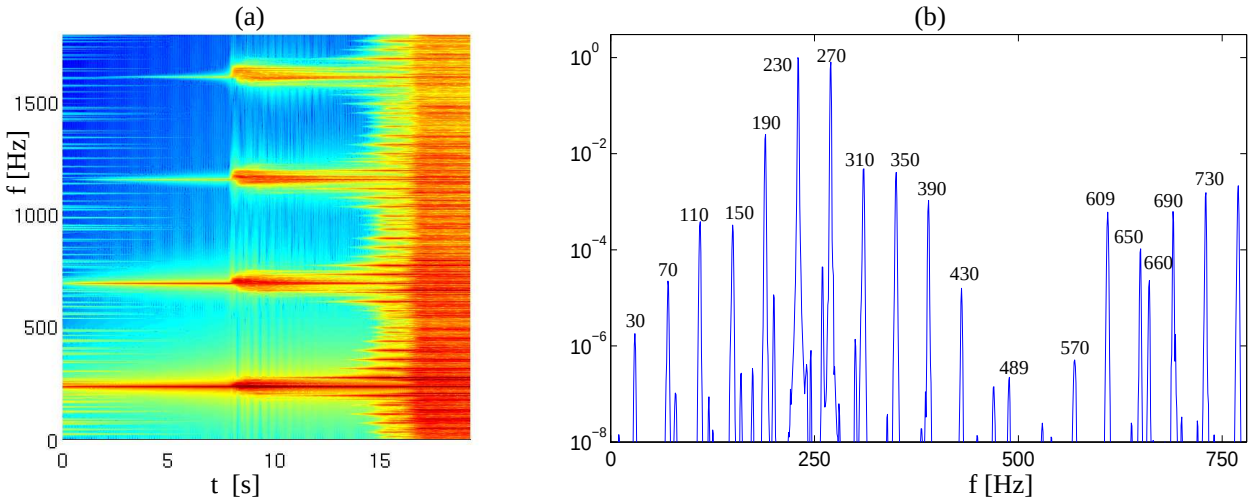


Figure 11: (a): Spectrogram of the vibration $w^{out}$ for the perfect plate excited at 230 Hz, with a forcing amplitude $F$ from 0 to 110 N in 20 seconds. (b): Fourier transform of 1.3 sec of the displacement at t=15 s.

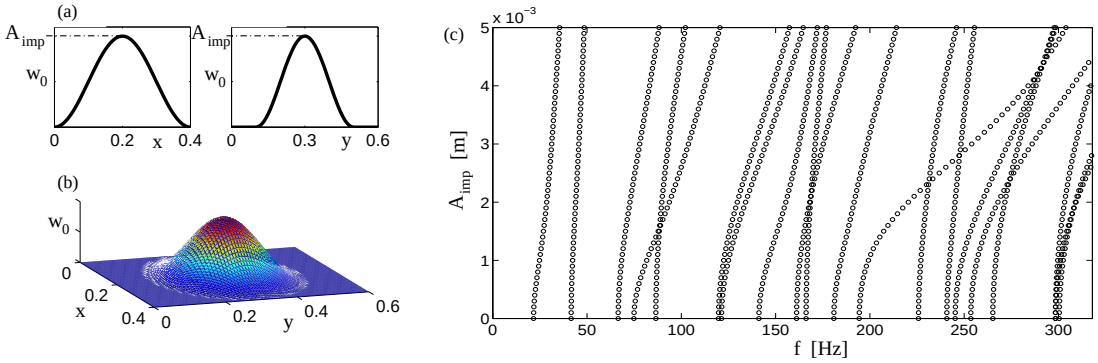


Figure 12: (a): cross-section (in the $x$ and $y$ directions) of the imperfection of amplitude $A_{imp}$ (in m) considered for the plate. (b): three-dimensional view of the imperfect plate. (c) : eigenfrequencies (in Hz) for increasing values of $A_{imp}$.

where $A_{imp}$ is the height (in m) of the imposed static deflection, and $L_{imp}$ its width. The imperfection is centered at $(x_0, y_0)$, as is shown in Fig. 12(a,b) for $x_0 = L_x/2$ and $y_0 = L_y/2$ which will be the case considered in the remainder of the study. All the other parameters (material parameters $\rho$, $E$ and $\nu$, size $L_x$, $L_y$ and thickness $h$) are unchanged with respect to the preceding case so as to illustrate a continuous deviation from the perfect case studied in preceding section. The width $L_{imp}$ has been set to 0.2 m.

A modal analysis can be conducted by considering the linear part of Eqs.(2):

$$\rho h \ddot{\bar{w}} + D\Delta\Delta\bar{w} = L(\bar{w}_0, \bar{F}), \tag{30a}$$

$$\Delta\Delta\bar{F} = -EhL(\bar{w}, \bar{w}_0), \tag{30b}$$

The associated eigenproblem is solved by using the finite-difference operators introduced in section 2. For increasing values of the imperfection amplitude $A_{imp}$ from 0 to 5 mm, the evolution of the eigenfrequencies is shown in Fig. 12(c). In the remaining cases, the value $A_{imp}$=1mm

(equal to the thickness) is chosen for the simulations. Table 4 gives the first 18 eigenfrequencies for this case, computed with $f_S$=50 kHz ($N_x$=36, $N_y$=54), *i.e.* the sampling frequency used for the dynamical simulations.

| | | | | | | | | |
|---|---|---|---|---|---|---|---|---|
| 24.81 | 42.34 | 68.33 | 81.63 | 87.24 | 122.35 | 124.78 | 145.78 | 162.56 |
| 166.49 | 184.10 | 198.76 | 226.42 | 241.67 | 247.69 | 255.65 | 265.61 | 298.38 |

Table 4: Eigenfrequencies for the imperfect plate chosen for the simulations, computed with $N_x$=36, $N_y$=54 spatial points ($f_S$=50 kHz). Dimensions are: $L_x$ = 0.4m, $L_y$ = 0.6m, $h$=1 mm, $A_{imp}$=1mm, $L_{imp}$ = 0.2 m, material parameters are: $E$= 200 GPa, $\nu$=0.3 and $\rho$=7860 kg.m$^{-3}$.

### *4.2. Transition scenario*

As compared to the perfect plate, the distinction between low and high frequencies does not appear in the simulations conducted. This appears naturally as a reflection of the fact that adding quadratic nonlinearity enables more simple order-two internal resonance relationships so that the scenario with the quasiperiodic state appears for the very first frequencies. A set of 24 simulations has been conducted for $f^{exc}$ ranging from 25 Hz (second mode) to 202 Hz, in the vicinity of the 12$^{\text{th}}$ mode (eigenfrequency at 199.25 Hz), *i.e.* in a somewhat narrower frequency band than for the perfect plate. The list of the frequencies tested (and in parenthesis the observed scenario: D for direct transition, QP for appearance of the quasiperiodic state (the resonance relationship is indicated when it was evident otherwise nothing is mentioned indicating that a single resonance could not be identified), MI for the last case where the direct transition is not clearly marked, as in the perfect case, as well as the critical force amplitude $\bar{A}_{cr}$ (in N) for which the turbulent behaviour sets in) is: 26 Hz (D, 20 N), 42 Hz (D, 45 N), 70 Hz (D, 10 N), 81 Hz (D, 15 N), 84 Hz (QP, 8 N), 85.5 Hz (QP, 1:2 case, 10 N), 87 Hz (QP, 1:2, 11 N), 92 Hz (D, 20 N), 109 Hz (QP, 62 N), 111 Hz (D, 60 N), 120 Hz (D, 58 N), 123 Hz (MI, 54 N), 130 Hz (QP, 12 N), 137 Hz (MI, 24 N), 140 Hz (D, 25 N), 142 Hz (D, 21 N), 147 Hz (MI, 10 N), 150 Hz (QP, 22 N), 160 Hz (QP, 1+1:2, 46 N), 162 Hz (QP, 44 N), 164 Hz (QP, 42 N), 167 Hz (QP, 45 N), 180 Hz (QP, 1:2, 35 N), 202 Hz (MI, 14 N). Hence in the 24 simulations run, only 9 direct transitions are observed, which is markedly in contrast with the perfect plate. It is thus concluded that the presence of quadratic nonlinearity favours the mode coupling and the appearance of energy exchange leading to a quasiperiodic state, which can be more easily degenerated in this case due to occurrences of 1:2 resonance.

Fig. 13 shows the simulation results obtained for $f^{exc}$=85.5 Hz. The 1:2 internal resonance is activated for very small values of the forcing amplitude. The coupling is with the second mode, the eigenfrequency of which is 42 Hz. One may also note the appearance of all even harmonics of the forcing frequency, in accordance with the presence of the quadratic nonlinearity. The coupled regime where the two modes are present in the vibration persists until the forcing amplitude attains the value of $\bar{A}$= 12 N, a smaller value for obtaining the turbulent regime as compared to those observed for the perfect plate. This is in accordance with numerical results presented in [25].

A more complicated case is now analyzed for $f^{exc}$=109 Hz, presented in Fig. 14. The spectrogram and the Fourier spectrum of the displacement shown in Fig. 14(b) indicate that a first energy transfer follows from 1+1:2 internal resonance. The modes number 1 and 4, whose eigenfrequency are respectively 24.8 and 81.6 Hz, are excited and slightly shifted so as to perfectly fulfill the relationship $f_1 + f_4 = f^{exc}$, with $f_1$=26.3 Hz, and $f_4$=82.7 Hz. The other

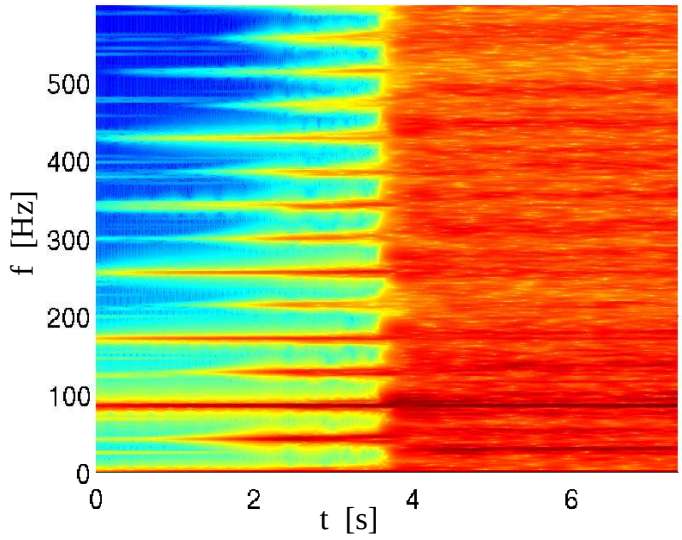


Figure 13: Spectrogram of output for the imperfect plate excited at 85.5 Hz, with a forcing amplitude $F$ from 0 to 60 N in 20 seconds (with only the first 8 seconds shown). A clear 1:2 internal resonance is excited for $F$=4 N before the turbulent regime sets in for $F$=12 N.

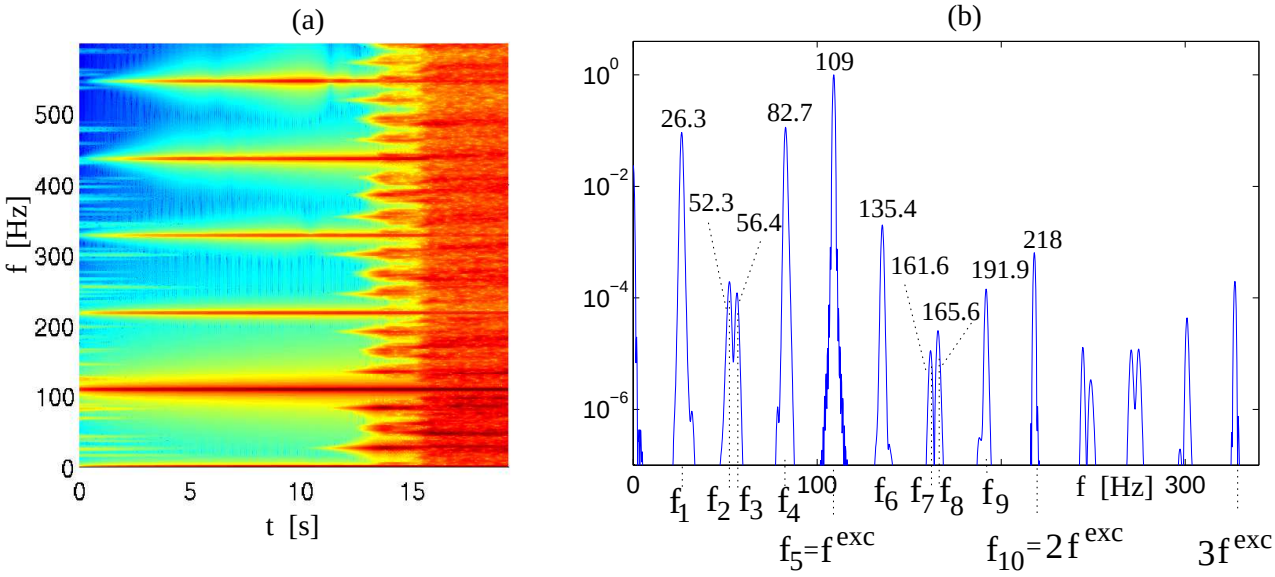


Figure 14: (a) Spectrogram of output for the imperfect plate excited at 109 Hz, with a forcing amplitude $F$ from 0 to 50 N in 20 seconds. (b) Fourier transform of 1.3 sec of the displacement $w^{out}$ at t=14 s, showing the combination resonances before the turbulent behaviour.

frequencies noted in the Fourier spectrum are denoted as: $f_2$=52.3 Hz, $f_3$=56.4 Hz, $f_5=f^{exc}$=109 Hz, $f_6$=135.4 Hz, $f_7$=161.6 Hz, $f_8$=165.6 Hz, $f_9$=191.9 Hz, $f_{10}=2f^{exc}$=218 Hz. Inspecting the internal resonance relationships existing over this set of frequencies, one can see that the

following order-two resonance relationships are fulfilled:

$$f_1 + f_3 = f_4, \tag{31a}$$
$$f_1 + f_8 = f_9, \tag{31b}$$
$$f_3 + f_7 = f_{10}. \tag{31c}$$

These three relations allows and explanation for energy transfer and the appearance of frequency peaks $f_3$, $f_8$, $f_9$ and $f_7$. Finally $f_2$ and $f_6$ are not involved in any order-two relationships. Thus we assume here that the presence of these frequency peaks is due to order-three internal resonance relationships, as one can verify that:

$$f_2 = f_7 + f_4 - f_9, \tag{32a}$$
$$f_6 = f_7 + f_9 - f_{10}. \tag{32b}$$

To conclude with this section, the distinction between low frequency and high frequency range for the imperfect plate has no meaning anymore since the generic transition scenario with the quasiperiodic state is the most frequently observed. The particular case of the perfect plate, unreachable in real experiments, enforces to make this distinction due to the lack of possible internal resonance that must mandatory be of order-three, and thus more difficult to activate. As soon as a small imperfection is considered (here equal to the thickness $h$), quadratic non-linearity is at hand, and energy transfer through quadratic couplings are more easily obtained. These numerical results confirms in particular that the imperfect plate is more likely to undergo instabilities for low levels of vibratory energy, as already shown in [25].

## 5. Turbulent behaviour

### *5.1. Wave Turbulence*

In this section, we analyze the regime occurring after the second bifurcation and characterized by a broadband Fourier spectrum. Recently, theoretical and experimental studies have revealed that the correct framework for analysis is that of a weakly turbulent behaviour, corroborating preliminary experimental studies revealing the divergence of dimension calculations when using classical indicators of low-dimensional chaos [23, 13]. Düring *et al* apply the Wave Turbulence Theory (WTT) to von Kármán equations of motions governing the non linear dynamics of thin plates, showing the existence of a direct cascade of energy through lengthscales and deriving their statistical properties in terms of energy repartition [26]. In particular, they show that the power spectrum $P_w(k)$ for the displacement $w$, for a perfect plate, must verify the following dependence:

$$P_w(k) = C\frac{P^{1/3}}{[12(1-\nu^2)]^{1/6}}\frac{\ln^{1/3}(k_\star/k)}{\sqrt{E/\rho}\,k^4}, \tag{33}$$

where $C$ is a constant, $P$ is the injected power, and $k = \|\mathbf{k}\|$ the modulus of the two-dimensional wavenumber. Omitting the log-dependence that is neglectable before the $k^{-4}$ one, and translating the theoretical prediction in the frequency domain and for the velocity $\dot{w}$, one obtains:

$$P_{\dot{w}}(f) = \frac{C' P^{1/3} h}{[12(1-\nu^2)]^{2/3}} f^0 \tag{34}$$

where the term $f^0$ has been written explicitly to underline the flat dependence as function of the frequency $f$. Experimental measurements reported in [27, 29, 28, 56, 57, 30] shows a

discrepancy between theory and experiments that is attributed to the presence of damping, not taken into account in the theoretical derivations.

Here we want to compare the results of our simulations with the predictions provided by WTT. Consequently, an undamped plate is selected so as to verify the energy repartition of the power spectrum given by (34). Note that in [26], a numerical scheme based on a pseudospectral method has already been used to validate the theoretical prediction.

Figure 15 shows a snapshot of the transverse displacement $w$ and velocity $\dot{w}$ for the plate excited with an amplitude of $A$=30 N and an excitation frequency of $f^{exc}$= 87 Hz, corresponding to Fig. 3. The spectrum of the displacement being $k$-dependent as $k^{-4}$, the snapshot of the displacement is quite smooth, while for the velocity higher frequencies are much more appreciable. This figure from numerical simulation can be compared to deformation and velocity measured experimentally and shown in [30].

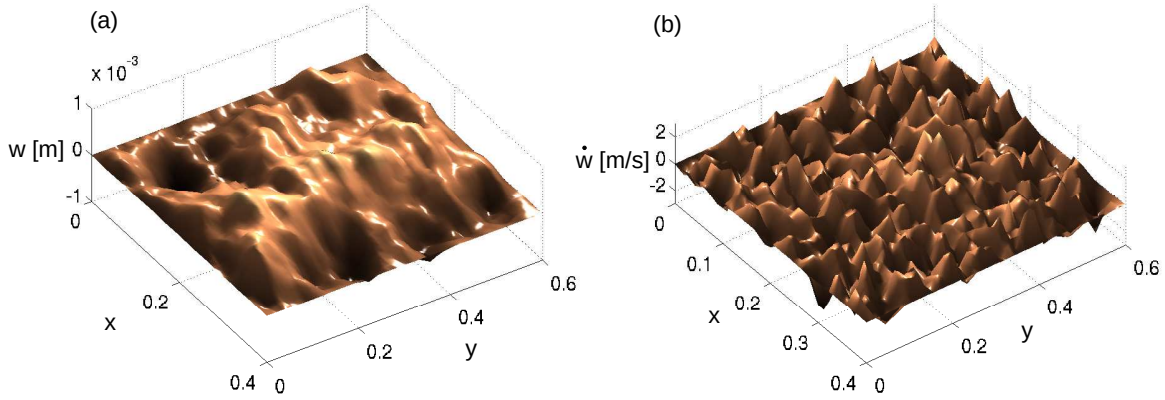


Figure 15: (a) Transverse displacement of the plate $w(x, y)$ in the turbulent regime. (b) Transverse velocity $\dot{w}(x, y)$. The undamped plate is excited at $f^{exc}$= 87 Hz with a forcing amplitude $A$=30 N.

### *5.2. Power spectra*

Numerical simulations of turbulent behaviour in conservative media are difficult because of the simultaneous presence of a cascade of energy (a priori infinite) from large to small lengthscales and the absence of dissipation in the system. As the energy flux enforces the creation of smaller and smaller lengthscales, a numerical problem is encountered when the Nyquist frequency, being half the sampling frequency $f_S$, is attained. From that, energy comes back into the simulation box as it should normally go to smaller lengthscales that are not simulated. Hence conducting numerical simulations in the undamped case requires, a priori, a very high value of $f_S$ in order to have a frequency band of interest where the cascade develops without numerical interference.

This is illustrated in Fig. 16, where the complete spectrograms of two simulations with the same set are shown, and for two different sampling frequency $f_S$. The undamped plate ($\sigma_0 = 0$) is excited with $f^{exc} = 75$ Hz, the amplitude of the forcing being increased from 0 to 80 N in two seconds, then kept constant during 8 seconds and finally cut off until the end of the simulation. In Figs 16(a-c), the sampling frequency is $f_S$= 100 kHz, while in Figs 16(b-d) it has been set to 400 kHz. The spectrograms are shown from 0 to the Nyquist frequency. The scheme itself

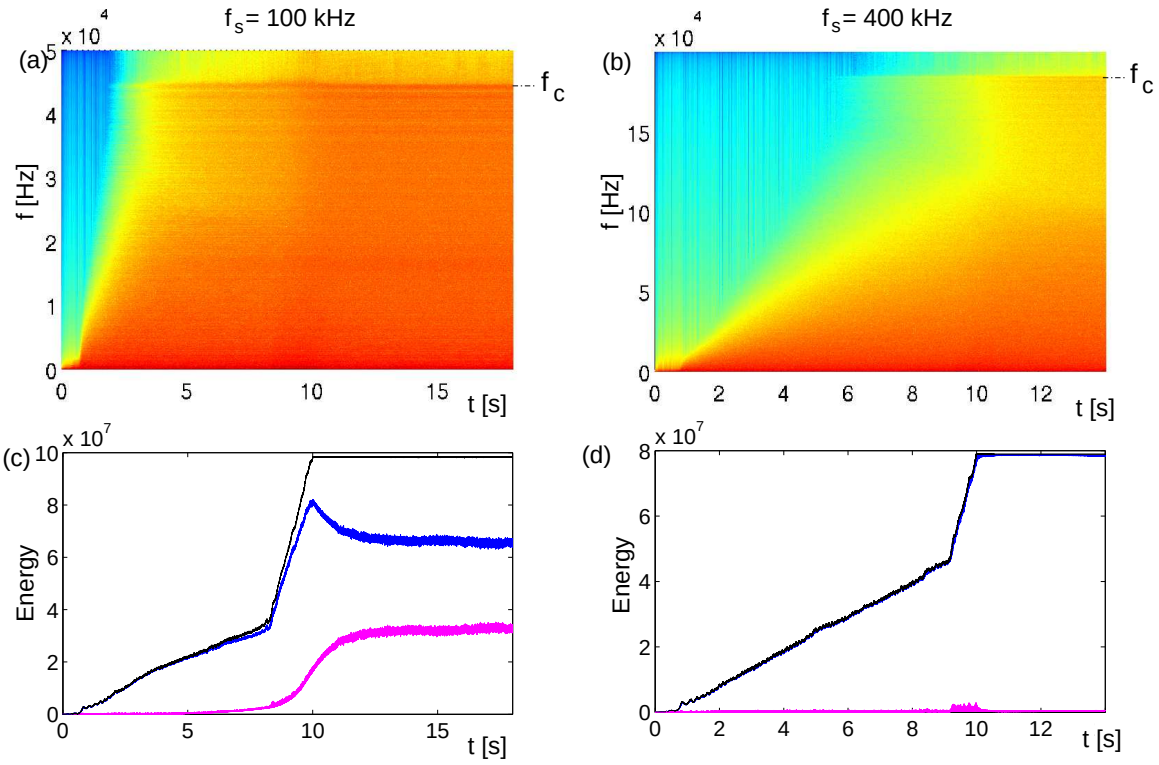


Figure 16: Spectrograms and Energies for the undamped plate excited at $f^{exc} = 75$ Hz. (a)-(c): $f_S = 100$ kHz, (b)-(d): $f_S = 400$ kHz. Bending energy in blue, in-plane energy in magenta, total energy in black.

exhibits a numerical cut-off, at:

$$f_C = \frac{f_S}{\pi}\text{Arcsin}\left(\frac{2\kappa}{f_S}\frac{(h_x^2 + h_y^2)}{h_x^2 h_y^2}\right) \tag{35}$$

In the limit of high sample rate, and if the grid spacings are chosen exactly according to the stability condition, this cutoff is precisely the Nyquist frequency $f_S/2$; in practice, however, there will be a slight loss of bandwidth due to a choice of grid spacings away from this bound (so, e.g., one may have the domain divided evenly into an integer number of grid points along each dimension).

For $f_S = 100$ kHz, one can observe that the upper frequency generated by the cascade quickly attains the Nyquist frequency. Due to the numerical limitation, the energy seems to be blocked in the very high frequency range, and starts to accumulate. Hence from that point, the computed solutions are not physical anymore, and what is observed is due to numerical limitations. This is also clearly seen on the energies. For $f_S = 100$ kHz, on can see in Fig. 16(c) that up to 5 seconds, the total energy increases linearly, the in-plane energy being maintained at a neglectable value. Then this in-plane energy starts to increase slowly and dramatically, with an evident broke-up in the slope of the total and bending energies. From that moment the numerical solutions are non physical anymore. What is observed is a sort of thermalization where the system relaxes to an absolute equilibrium state completely driven by the numerical limitation. Similar numerical observations are shown for Euler flows in turbulent regime [58].

For $f_S = 400$ kHz, the time for the energy flux to generate an upper frequency attaining the Nyquist frequency is enough so that the numerical results can be taken as reliable, until $t$= 9

seconds, where the slope of the energy is suddenly broken. From that point, one can see that the in-plane energy starts to increase slowly, whereas the bending one starts to slowly decrease. If the simulation have been ran on a longer time, the final state reached by the system would have been the same as that observed for $f_S = 100$ kHz. A simulation realized with $f_S = 200$ kHz confirms the scenario by showing an intermediate stage. Hence for obtaining reliable results in the undamped case, a very high value of $f_S$ has to be selected, which renders the computation extremely long. For $f_S = 400$ kHz and the plate selected, the number of grid points was $N_x = 102$ and $N_y = 154$, and the simulation time was 4 weeks on a standard PC.

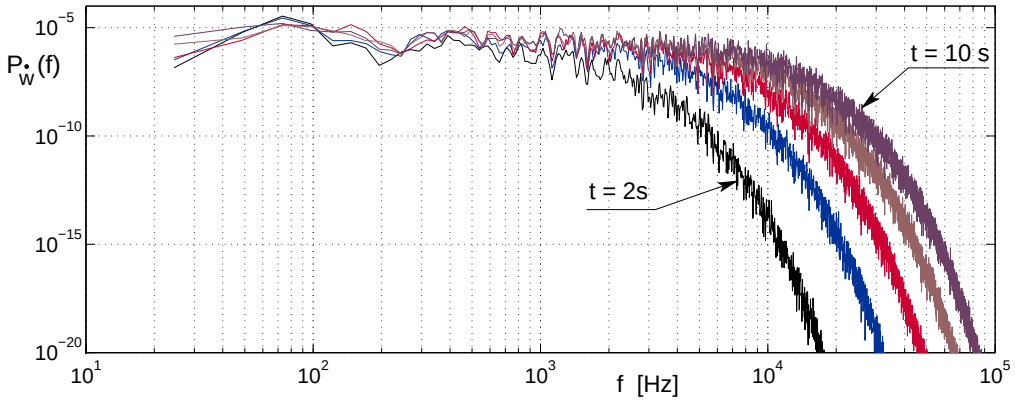


Figure 17: Power spectra of the velocity, for the simulation with $f_S = 400$ kHz, and at successive instants, respectively: $t$= 2s, 4s, 6s, 8s and 10 s. Power spectra are compute with windows of 16384 points (0.041 s), mean-valued over twelve successive windows so that 0.5 seconds of signal is used at each instant.

The simulation with $f_S = 400$ kHz has been used so as to verify the prediction of WTT on the power spectra of the transverse velocity, Eq. (34). As can be seen in Figure 17, a clear cascade regime sets in with a power law of $f^0$ being verified over more than two decades, showing the robustness of the numerical method used. It has also been verified that the problem encountered and discussed for the undamped case disappears as soon as one adds damping to the simulation. In this case, the cascade does not extend to infinity and energy is dissipated until the energy flux attains the Nyquist frequency, provided the sampling frequency is chosen high enough.

## 6. Conclusion

The transition from periodic to wave turbulence regime in the forced vibrations of thin plates has been presented. Experimental results, described in the introduction, reveal that a generic transition scenario can be inferred. A detailed numerical study on a simply supported plate has been here proposed, hence completing the results presented on free-edge circular plates in [25], and assessing the transition scenario involving at most two bifurcations. The first one implies a loss of stability of the directly excited mode in favour of a coupled regime where the energy is shared between a rather small subset of internally resonant modes. The resulting motion is generally quasiperiodic but can degenerate to periodic in case of very simple internal resonance, *e.g.* 1:2 or 1:3. The second bifurcation is characterized by the loss of stabililty of this coupled regime and the appearance of wave turbulence. This scenario may also degenerate and simplify to a direct transition from periodic to turbulent motions if no simple energy exchange through internal resonances can be activated.

For perfect plates, direct transitions are generally observed for the first eigenmodes, whereas the complete three-stages scenario is the most frequently observed from the $20^{th}$ mode approximately. This is a reflection of the fact that perfect plates can exchange energy only through third-order internal resonance relationships that are more difficult to activate. On the other hand, for imperfect plates displaying quadratic nonlinearity, the complete scenario has been numerically found from the very first modes, in the line of experimental observations. The numerical results have also revealed that internal resonance relationships may not be directly deduced from the natural frequencies, because of the frequency shifts due to geometric nonlinearity for increasing energies. The observed internal resonances sometimes involved frequency peaks being far from the linear values, so that a prediction of the involved couplings after the first bifurcation needs to be done on the basis of a frequency-energy plot, representing the variations of the NNM frequencies with respect to the energy level. Finally, the case of a transition involving a rapid though markedly broadening of the spectral harmonics of the excitation, has been found for some frequencies; a case that has also been observed experimentally. The bifurcation shares common features with the modulation instability that could be the dynamical phenomena at work to transite to turbulence, but a complete characterization needs further research that is postponed to future work. After the second bifurcation, wave turbulence sets in; and it has been numerically verified that power spectra of the computed velocity fulfills the theoretical predictions given by WT for von Kármán dynamical equations for perfect undamped plates.

## Acknowledgments

The authors want to thank Arezki Boudaoud and Olivier Thomas for numerous discussions related to the turbulent behaviour of vibrating plates. Loris Longo Mucciante is also thanked for preliminary simulations realized with free-edge boundary conditions.

## References

[1] U. Frisch, Turbulence, Cambridge University Press, 1995.

[2] P. Manneville, Dissipative structures and weak turbulence, Academic Press, 1990.

[3] V. E. Zakharov, V. S. Lvov, G. Falkovisch, Kolmogorov Spectra of Turbulence I: Wave Turbulence, Springer Verlag, Berlin, 1992.

[4] A. Newell, S. Nazarenko, L. Biven, Wave turbulence and intermittency, Physica D 152-153 (2001) 520–550.

[5] V. E. Zakharov, N. N. Filonenko, Energy spectrum for stochastic oscillations of surface of a liquid, Journal of Applied Mechanics and Technical Physics 8 (5) (1967) 37–40.

[6] A. N. Pushkarev, V. E. Zakharov, Turbulence of capillary waves, Physical Review Letters 76 (1996) 3320–3323.

[7] A. I. Dyachenko, A. O. Korotkevich, V. E. Zakharov, Weak turbulent Kolmogorov spectrum for surface gravity waves, Physical Review Letters 92 (13) (2004) 134501.

[8] E. Falcon, C. Laroche, S. Fauve, Observation of gravity-capillary wave turbulence, Physical Review Letters 98 (2007) 094503.

[9] S. L. Musher, A. M. Rubenchik, V. E. Zakharov, Weak Langmuir turbulence, Physics Reports 252 (4) (1995) 177–274.

[10] S. Dyachenko, A. C. Newell, A. Pushkarev, V. E. Zakharov, Optical turbulence: weak turbulence, condensates and collapsing filaments in the nonlinear schrdinger equation, Physica D 57 (1-2) (1992) 96–160.

[11] S. V. Nazarenko, A. C. Newell, S. Galtier, Non-local MHD turbulence, Physica D 152-153 (2001) 646–652.

[12] C. Touzé, A. Chaigne, T. Rossing, S. Schedin, Analysis of cymbal vibrations using non-linear signal processing tools, in: Proceedings of the International Symposium on Musical Acoustics, Leavenworth, USA, 1998, pp. 377–382.

[13] C. Touzé, A. Chaigne, Lyapunov exponents from experimental time series: application to cymbal vibrations, Acta Acustica 86 (3) (2000) 557–567.

[14] A. Chaigne, C. Touzé, O. Thomas, Nonlinear vibrations and chaos in gongs and cymbals, Acoustical Science and Technology, Acoustical Society of Japan 26 (5) (2005) 403–409.

[15] N. H. Fletcher, T. D. Rossing, The Physics of musical instruments, Springer, New-York, 1998, second edition.

[16] S. Bilbao, Numerical Sound synthesis: Finite Difference Schemes and Simulation in Musical Acoustics, Wiley, 2009.

[17] K. Legge, N. H. Fletcher, Nonlinearity, chaos, and the sound of shallow gongs, Journal of the Acoustical Society of America 86 (6) (1989) 2439–2443.

[18] J. Awrejcewicz, V. A. Krysko, A. V. Krysko, Spatio-temporal chaos and solitons exhibited by von Kármán model, International Journal of bifurcation and Chaos 12 (7) (2002) 1465–1513.

[19] J. Awrejcewicz, V. A. Krysko, I. V. Papkova, Chaotic vibrations of sector-type spherical shells, ASME Journal of Computational and Nonlinear Dynamics 3 (4) (2008) 041005, doi:10.1115/1.2908134.

[20] K. Nagai, S. Maruyama, M. Oya, T. Yamaguchi, Chaotic oscillations of a shallow cylindrical shell with a concentrated mass under periodic excitation, Computers and Structures 82 (2004) 2607–2619.

[21] K. Nagai, S. Maruyama, T. Murata, T. Yamaguchi, Experiments and analysis on chaotic vibrations of a shallow cylindrical shell-panel, Journal of Sound and Vibration 305 (2007) 492–520.

[22] S. Maruyama, K. Nagai, Y. Tsuruta, Modal interactions in chaotic vibrations of a shallow double-curved shell-panel, Journal of Sound and Vibration 315 (2008) 607–625.

[23] K. D. Murphy, L. N. Virgin, S. A. Rizzi, Characterizing the dynamic response of a thermally loaded, acoustically excited plate, Journal of Sound and Vibration 196 (5) (1996) 635–658.

[24] C. Touzé, Analyse et modélisation de signaux acoustiques et vibratoires chaotiques. application aux intruments de percussion non-linéaires (analysis and modelisation of vibratory and acoustics chaotic signals. Application to nonlinear percussion instruments), Ph.D. thesis, Université Pierre et Marie Curie, Paris VI (2000).

[25] C. Touzé, O. Thomas, M. Amabili, Transition to chaotic vibrations for harmonically forced perfect and imperfect circular plates, International Journal of Non-linear Mechanics 46 (1) (2011) 234–246.

[26] G. Düring, C. Josserand, S. Rica, Weak turbulence for a vibrating plate: Can one hear a Kolmogorov spectrum?, Physical Review Letters 97 (2006) 025503.

[27] A. Boudaoud, O. Cadot, B. Odille, C. Touzé, Observation of wave turbulence in vibrating plates, Physical Review Letters 100 (2008) 234504.

[28] O. Cadot, A. Boudaoud, C. Touzé, Statistics of power injection in a plate set into chaotic vibration, European Physical Journal B 66 (2008) 399–407.

[29] N. Mordant, Are there waves in elastic wave turbulence ?, Physical Review Letters 100 (2008) 234505.

[30] N. Mordant, Fourier analysis of wave turbulence in a thin elastic plate, European Physical Journal B 76 (2010) 537–545.

[31] O. Thomas, Analyse et modélisation de vibrations non-linaires de milieux minces élastiques. application aux instruments de percussion (analysis and modelisation of nonlinear vibrations of thin elastic media. Application to nonlinear percussion instruments), Ph.D. thesis, Université Pierre et Marie Curie, Paris VI (2001).

[32] S. Bilbao, A family of conservative finite difference schemes for the dynamical von Kármán plate equations, Numerical Methods for Partial Differential Equations 24 (1) (2007) 193–216.

[33] C. Touzé, S. Bilbao, L. Longo-Mucciante, O. Cadot, A. Boudaoud, Vibrations chaotiques de plaques minces: application aux instruments de type cymbale (chaotic vibrations of thin plates: application to cymbal-like instruments), in: Proceedings of the $10^{th}$ French Congress on Acoustics (CFA 2010), Lyon, France, 2010.

[34] A. Chaigne, C. Touzé, O. Thomas, Non-linear axisymmetric vibrations of gongs, in: Proceedings of the International Symposium on Musical Acoustics, Perugia, Italy, 2001.

[35] O. Thomas, C. Touzé, A. Chaigne, Asymmetric non-linear forced vibrations of free-edge circular plates, part II: experiments, Journal of Sound and Vibration 265 (5) (2003) 1075–1101.

[36] O. Thomas, C. Touzé, E. Luminais, Non-linear vibrations of free-edge thin spherical shells: experiments on a 1:1:2 internal resonance, Nonlinear Dynamics 49 (1-2) (2007) 259–284.

[37] C. Camier, C. Touzé, O. Thomas, Non-linear vibrations of imperfect free-edge circular plates and shells, European Journal of Mechanics A/Solids 28 (2009) 500–515.

[38] A. H. Nayfeh, D. T. Mook, Nonlinear oscillations, John Wiley & sons, New-York, 1979.

[39] A. H. Nayfeh, Nonlinear interactions: analytical, computational and experimental methods, Wiley series in nonlinear science, New-York, 2000.

[40] O. Thomas, C. Touzé, A. Chaigne, Non-linear vibrations of free-edge thin spherical shells: modal interaction rules and 1:1:2 internal resonance, International Journal of Solids and Structures 42 (11-12) (2005) 3339–3373.

[41] C. Touzé, O. Thomas, A. Chaigne, Asymmetric non-linear forced vibrations of free-edge circular plates, part I: theory, Journal of Sound and Vibration 258 (4) (2002) 649–676.

[42] M. Amabili, Nonlinear vibrations and stability of shells and plates, Cambridge University Press, 2008.

[43] G. Ostiguy, S. Sassi, Effects of initial imperfections on dynamic behaviour of rectangular plates, Non-linear Dynamics 3 (1992) 165–181.

[44] A. W. Leissa, Vibration of plates, Acoustical Society of America, 1993, (orig. issued NASA SP-160, 1969).

[45] O. Thomas, S. Bilbao, Geometrically nonlinear flexural vibrations of plates: In-plane boundary conditions and some symmetry properties, Journal of Sound and Vibration 315 (3) (2008) 569–590.

[46] R. Lewandowski, Computational formulation for periodic vibration of geometrically nonlinear structures, part I: theoretical background, International Journal of Solids and Structures 34 (1997) 1925–1947.

[47] R. Lewandowski, Computational formulation for periodic vibration of geometrically nonlinear structures, part II: numerical strategy and examples, International Journal of Solids and Structures 34 (1997) 1949–1964.

[48] G. Kerschen, M. Peeters, J. Golinval, A. Vakakis, Non-linear normal modes, part I: a useful framework for the structural dynamicist, Mechanical Systems and Signal Processing 23 (1) (2009) 170–194.

[49] M. Peeters, R. Viguié, G. Sérandour, G. Kerschen, J. Golinval, Non-linear normal modes, part II: toward a practical computation using numerical continuation techniques, Mechanical Systems and Signal Processing 23 (1) (2009) 195–216.

[50] A. Vakakis, O. Gendelman, L. Bergman, D. McFarland, G. Kerschen, Y. Lee, Nonlinear targeted energy transfer in mechanical and structural systems I, Springer, New-York, 2008.

[51] U. Parlitz, W. Lauterborn, Superstructure in the bifurcation set of the Duffing equation, Physics Letters A 107 (8) (1985) 351–355.

[52] W. Szemplinska-Stupnicka, The behavior of nonlinear vibrating systems, vol. I: fundamental concepts and methods. Application to single-degree-of-freedom systems, Kluwer Academic Publishers, Dordrecht, 1990.

[53] V. E. Zakharov, L. A. Ostrovsky, Modulation instability: the beginning, Physica D 238 (5) (2009) 540–548.

[54] I. Daumont, T. Dauxois, M. Peyrard, Modulation instability: first step towards energy localization in nonlinear lattices, Nonlinearity 10 (3) (1997) 617–630.

[55] H. Xia, M. Shats, H. Punzmann, Modulation instability and capillary wave turbulence, Europhysics letters 91 (1) (2010) 14002.

[56] P. Cobelli, P. Petitjeans, A. Maurel, V. Pagneux, N. Mordant, Space-time resolved wave turbulence in a vibrating plate, Physical Review Letters 103 (2009) 204301.

[57] O. Cadot, C. Touzé, A. Boudaoud, Linear versus nonlinear response of a forced wave turbulence system, Physical Review E 82 (2010) 046211.

[58] C. Cichowlas, P. Bonaïti, F. Debbasch, M.-E. Brachet, Effective dissipation and turbulence in spectrally truncated Euler flows, Physical Review Letters 95 (2005) 264502.